8-26-2019

Cislunar Trajectory Generation with Sun-Exclusion Zone Constraints Using a Genetic Algorithm and Direct Method Hybridization

Joshua A. Ostman

Recommended Citation

Ostman, Joshua A., "Cislunar Trajectory Generation with Sun-Exclusion Zone Constraints Using a Genetic Algorithm and Direct Method Hybridization" (2019). *Theses and Dissertations*. 2373.
https://scholar.afit.edu/etd/2373

CISLUNAR TRAJECTORY GENERATION WITH SUN-EXCLUSION ZONE CONSTRAINTS USING A GENETIC ALGORITHM AND DIRECT METHOD HYBRIDIZATION

THESIS

Joshua A. Ostman

AFIT-ENY-MS-19-S-081

DEPARTMENT OF THE AIR FORCE
AIR UNIVERSITY

AIR FORCE INSTITUTE OF TECHNOLOGY

Wright-Patterson Air Force Base, Ohio

AFIT-ENY-MS-19-S-081

CISLUNAR TRAJECTORY GENERATION WITH SUN-EXCLUSION ZONE CONSTRAINTS USING A GENETIC ALGORITHM AND DIRECT METHOD HYBRIDIZATION

THESIS

Presented to the Faculty
Department of Astronautical Engineering
Graduate School of Engineering and Management
Air Force Institute of Technology
Air University
Air Education and Training Command
in Partial Fulfillment of the Requirements for the
Degree of Master of Science in Astronautical Engineering

Joshua A. Ostman, B.S.A.A.E.

August 26, 2019

AFIT-ENY-MS-19-S-081

CISLUNAR TRAJECTORY GENERATION WITH SUN-EXCLUSION ZONE CONSTRAINTS USING A GENETIC ALGORITHM AND DIRECT METHOD HYBRIDIZATION

THESIS

Joshua A. Ostman, B.S.A.A.E.

Committee Membership:

Maj Joshuah Hess, Ph.D.
Chair

Lt Col Kirk Johnson, Ph.D.
Member

Maj Costantinos Zagaris, PhD
Member

Table of Contents

Page

List of Figures

Figure Page

List of Tables

AFIT-ENY-MS-19-S-081

Abstract

Space missions to the Moon have received renewed interest in recent decades. Science missions continue to be sent to the Moon, and several space agencies have aspirations of establishing a human presence on the Moon. With the increased number of artificial objects in cislunar space, the problem of tracking these objects arises. Optical sensors are able to track these objects in deep space. However, optical sensors cannot track objects that are close to the Sun as viewed from the observer. This unobservable region is the Sun-exclusion zone (SEZ). This research attempts to create optimal Moon-Earth transfers which are completely in the SEZ using a genetic algorithm–direct method hybridization. Such transfers demonstrate how much the SEZ can limit optical sensors from maintaining custody of a satellite. Transfers from L_1 and L_2 Lyapunov orbits to geosynchronous orbit are generated while optimizing fuel and time of flight. Remaining inside of the SEZ is shown to significantly increase the fuel required to make the transfer.

Acknowledgements

I would first like to thank my adviser for all of his guidance and expertise. Maj Hess was extremely helpful in preparing me to do research in the area I was interested.

I would like to thank my employer for giving me the opportunity to pursue a degree at AFIT.

I would like to thank my family and Stephanie for all of their love and support.

Joshua A. Ostman

CISLUNAR TRAJECTORY GENERATION WITH
SUN-EXCLUSION ZONE CONSTRAINTS USING A GENETIC ALGORITHM
AND DIRECT METHOD HYBRIDIZATION

I. Introduction

1.1 Background and Motivation

The U.S. has benefited from leadership in space economically, militarily, and scientifically [2]. U.S. forces depend on space for Pointing, Navigation, and Timing (PNT); Space Situational Awareness (SSA); Intelligence, Surveillance, and Reconnaissance (ISR); and satellite communications (SATCOM) [3]. With a dependence on space, our assets in space become a potential vulnerability.

A constant threat to U.S. assets in space includes collision with man-made objects, like space debris or other satellites. The 2007 test of a Chinese destructive anti-satellite (ASAT) system [2] is an example of both the passive and active potential threat. The guided anti-satellite weapon is an active threat, intentionally intercepting the path of a satellite. The 3,000 pieces of debris [3] left by the collision illustrates the passive threat. Countries continue to pursue anti-satellite weapons, perceiving the U.S. assets in space as a vulnerability [4].

The United States maintains the Space Surveillance Network (SSN) to track man-made objects orbiting the Earth [5]. One function of the SSN is to identify and track the active and passive threats in orbit. The SSN has a collection of radar and optical sensors. The Ground-based Electro-Optical Deep Space Surveillance (GEODSS) System, a part of the SSN, can track an object as small as a basketball in geosynchronous Earth orbit (GEO) [5]. This network is foundational for understanding the capabilities and intentions of other actors in space, and the DoD is committed to improving the quality and quantity of the information the SSN provides [2].

Although the United States is the leader in space situational awareness [2], there are natural limitations to the SSN. Weather conditions can limit the effectiveness of ground based optical systems [5]. Ground based optical systems are also limited to operating primarily at night [5]. Another limitation is the Sun-exclusion zone (SEZ). It is difficult for an optical sensor to detect a satellite when the satellite lies between the sensor and the Sun. The optical noise from the Sun limits the ability to detect the light emanating from the satellite body. A satellite in geosynchronous orbit is in the Sun-exclusion zone for about 6 hours a day for an observer at the Earth [6]. A satellite in an even higher orbit such as near the Moon will be in the Sun-exclusion zone for about 8 continuous days each month. A possible solution to remove Sun-exclusion zone outages may be to add high altitude sensors to the SSN [6].

These outages may limit the U.S. ability to quickly observe new space debris. The outages could also mask the movement of reconstitution satellites from a parking orbit to a desired conventional orbit [7]. Outages could restrict attribution of the movement of satellites, and therefore the ability to effectively respond to such activity [2].

1.2 CR3BP Environment

The most basic model in orbital mechanics is the two-body problem in which a smaller body with negligible mass orbits a larger body, such as a satellite in orbit about the Earth. The two-body problem has an analytical solution, which is desirable. However, when a second massive body is considered, the two-body approximation may not be valid for some applications. The circular restricted three body problem (CR3BP) models the gravitational effect on a satellite by two larger bodies in circular orbit about their common barycenter. An example of a system that could be reasonably modeled this way is the Earth-Moon system, with the Moon having an eccentricity of 0.0549.

No analytical solution to the CR3BP exists, and solutions need to be numerically integrated. The CR3BP is a chaotic system, meaning that small changes to the initial conditions can produce large effects to the state over elapsed time. Therefore, the CR3BP can be computationally expensive and seemingly unpredictable [8].

With the added complexity of modeling the CR3BP, there are also added benefits. The CR3BP is a more accurate model than the two-body problem for modeling cislunar trajectories because it accounts for the effects of both massive bodies simultaneously. The CR3BP provides insight into the Lagrange equilibrium points, locations where a smaller satellite remains fixed in a rotating reference frame. These equilibrium points have been used for science missions [9], and have been suggested to support Moon missions as staging areas and for providing communications [10].

One way to model a cislunar trajectory is patched conics. Patched conics assume an Earth two-body problem when a satellite is in the Earth's sphere of influence. When the satellite enters the Moon's sphere of influence, a Moon two-body problem is used. The two systems are patched when the satellite transitions from the Earth sphere to the Moon sphere. This technique ignores the use of invariant manifolds that exist in the CR3BP. Invariant manifolds come from dynamical systems theory, and are "superhighways" [11] that exist in the CR3BP, and are able to transport a satellite from the Earth sphere to the Moon sphere, or vice versa, with a very small amount of fuel. These manifolds are able to provide lower cost Earth-Moon transfers by using the natural CR3BP dynamics.

Satellites in higher altitude orbits, especially near the Moon, are at less risk from space debris compared to satellites at lower orbits. Cislunar space is less populated and costly to reach, making collisions with other satellites less likely. Using high altitude orbits and CR3BP dynamics may be useful for designing reconstitution satellites. Reconstitution satellites are satellites used to replace a degraded space capability. A reconstitution satellite could remain in orbit near the Moon until it is needed at a lower orbit.

1.3 Thesis Overview

The current research investigates the transfer of a satellite near the Moon (L_1 and L_2 Lyapunov orbits) to geosynchronous orbit while remaining inside of the Sun-exclusion zone for an optical sensor near the Earth. This will determine the effect of Sun-exclusion zone outages to observation of cislunar trajectories. The research uses a genetic algorithm and direct method hybridization to generate Pareto optimal solutions. The hybridization will optimize the time of the transfer and the fuel used. The research is designed to answer the following questions:

1. Can a genetic algorithm–direct method generate transfers from L_1 and L_2 Lyapunov orbits to geosynchronous orbit while optimizing fuel and time of flight?
2. What is the feasibility of making transfers from L_1 and L_2 Lyapunov orbits to GEO while enforcing a constraint that the transfer must remain inside of a Sun-exclusion zone?

To answer the research questions, the research is organized into the following:

- Chapter 2 will go over the background and characteristics of the CR3BP that are leveraged in this research. This will include the generation of periodic orbits, the state transition matrix, and invariant manifolds. A brief overview of genetic algorithms and trajectory optimization will also be included.

- Chapter 3 will cover the methodology for answering the research questions by laying out the test plans and solution algorithms. This chapter will discuss how the genetic algorithm–direct method hybridization is used to find Pareto optimal solutions and satisfy SEZ constraints.

- Chapter 4 will show and analyze the results following the methodology proposed in Chapter 3. The chapter will discuss how the technique performed in finding optimal solutions. The results for the transfer while remaining in the SEZ will be discussed.

- Chapter 5 will provide main conclusions to the work. Recommendations for future work will be provided.

II. Background

2.1 Chapter Overview

For designing optimal transfers from the L_1 and L_2 Lyapunov orbits to the Moon, the CR3BP is used to model the Earth-Moon system. This section gives the necessary background of the CR3BP as well as some of the tools and methods used when performing mission design in the CR3BP. The section also gives a brief overview of trajectory optimization.

2.2 The N-Body Problem

The CR3BP is a specialized case of the N-Body problem (NBP). The NBP is a system of N point masses, with the force acting on a particle being a combination of mutual gravitational attractions [12]. According to Newton's second law, the sum of the force on an object is equal to its mass times its acceleration, shown in Eq. (1). Newton's law of universal gravitation states that two objects attract each other along the line intersecting their center of masses with a force directly proportional to the product of their masses, and inversely proportional to the square of the distance between them, shown in Eq. (2). Combining Eq. (1) and Eq. (2) gives the equations of motion for the NBP in Eq. (3) [12]. The NBP is shown in Figure 1.

$$m\ddot{\vec{r}} = \sum \vec{F} \tag{1}$$

$$F = G\frac{m_1 m_2}{|\vec{r}|^2} \tag{2}$$

$$m_i\ddot{\vec{r}}_i = \sum_{j=1, j\neq i}^{N} \frac{G m_i m_j(\vec{r}_j - \vec{r}_i)}{|\vec{r}_j - \vec{r}_i|^3} \tag{3}$$

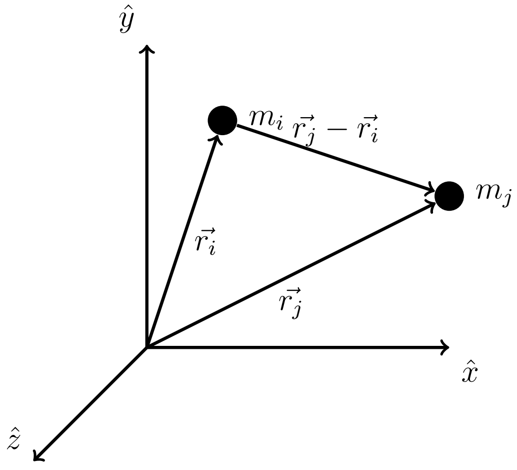

Figure 1. The N-body Problem

2.3 Circular Restricted Three Body Problem

The CR3BP is defined as two "primaries" that are in circular orbits about their common barycenter, and a third body being influenced by the gravity of the two primaries [13]. The three major assumptions of the CR3BP are [13]:

1.) The primary masses m_1 and m_2 are assumed to be point masses.

2.) The third body's mass is much smaller compared to the primaries (that is, $m_3 << m_1, m_2$) and does not influence the motion of m_1 and m_2.

3.) The two primary bodies are in circular orbits about their common barycenter.

The CR3BP models the motion of the third body under the influence of the two primary masses in a rotating reference frame. Starting with the EOMs of the NBP in Eq. (3), the acceleration on m_3 caused by m_1 and m_2 is shown in Eq. (4). The vectors used in Eq. (4) are shown in Figure 2.

$$m_3\ddot{\vec{r}}_3 = \frac{Gm_1m_3(\vec{r}_1 - \vec{r}_3)}{|\vec{r}_1 - \vec{r}_3|^3} + \frac{Gm_2m_3(\vec{r}_2 - \vec{r}_3)}{|\vec{r}_2 - \vec{r}_3|^3} \tag{4}$$

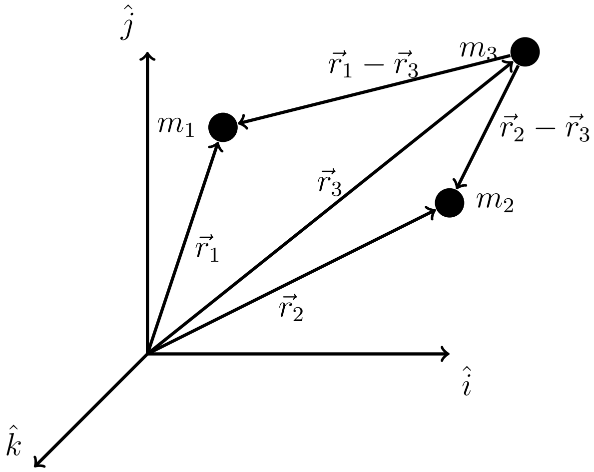

Figure 2. CR3BP in a Barycentric Inertial Reference Frame

The vectors $\vec{D}$ and $\vec{R}$ are introduced as:

$$\vec{D} = \vec{r}_3 - \vec{r}_1$$

$$\vec{R} = \vec{r}_3 - \vec{r}_2$$

Vector $\vec{r}_3$ is denoted as $\vec{p}$. The EOM for the third body is shown in Eq. (5).

$$\ddot{\vec{p}} = -\frac{Gm_1\vec{D}}{||\vec{D}||^3} - \frac{Gm_2\vec{R}}{||\vec{R}||^3} \tag{5}$$

The next step is to find the equations of motion in the CR3BP rotating reference frame, shown in Figure 3. The origin of the reference frame is the m_1, m_2 barycenter. The x-axis points in the direction of m_2, the z-axis extends in the direction of the angular momentum of the system, and the y-axis completes this right handed coordinate frame. The angular velocity of the CR3BP rotating reference frame with respect to an inertial frame will be $\vec{\omega}^{RI}$, the same angular velocity of the two bodies about their common barycenter. Since the two primary bodies are in circular orbits, this angular velocity is constant, and $\dot{\vec{\omega}}^{RI} = 0$. The transport theorem is used to find the EOMs in the rotating reference frame.

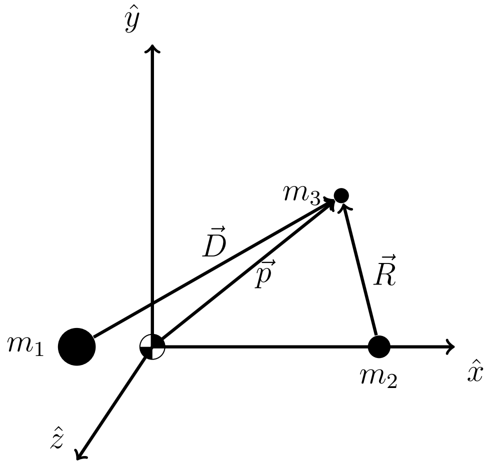

Figure 3. CR3BP Rotating Reference Frame

The transport theorem is defined in Eq. (6), where the I and R superscripts represent the inertial and CR3BP rotating reference frames, respectively.

$$ {}^{I}\frac{d}{dt}() = {}^{R}\frac{d}{dt}() + \vec{\omega}^{RI} \times () \tag{6} $$

By applying the transport theorem, the first and second derivatives of $\vec{p}$ in the inertial frame are

$$ {}^{I}\dot{\vec{p}} = {}^{R}\dot{\vec{p}} + \vec{\omega}^{RI} \times \vec{p} \tag{7} $$

$$ {}^{I}\ddot{\vec{p}} = {}^{R}\ddot{\vec{p}} + 2\vec{\omega}^{RI} \times {}^{R}\dot{\vec{p}} + \vec{\omega}^{RI} \times (\vec{\omega}^{RI} \times \vec{p}) \tag{8} $$

Substituting Eq. (8) into Eq. (5), gives the following

$$ {}^{R}\ddot{\vec{p}} = -2\vec{\omega}^{RI} \times {}^{R}\dot{\vec{p}} - \vec{\omega}^{RI} \times (\vec{\omega}^{RI} \times \vec{p}) - \frac{Gm_1\vec{D}}{||\vec{D}||^3} - \frac{Gm_2\vec{R}}{||\vec{R}||^3} \tag{9} $$

The vector $\vec{p}$ and the rotation $\vec{\omega}$ are defined in Eqs. (10) and (11). The rotation rate is the mean motion of the two primary bodies. In Eq (11), a represents the distance between the two primary bodies.

$$\vec{p} = X\hat{x} + Y\hat{y} + Z\hat{z} \tag{10}$$

$$\vec{\omega}^{RI} = N\hat{z} = \sqrt{\frac{G(m_1 + m_2)}{a^3}}\hat{z} \tag{11}$$

The cross products in Eq. (9) are performed.

$$\vec{\omega}^{RI} \times {}^{R}\dot{\vec{p}} = -N\dot{Y}\hat{x} + N\dot{X}\hat{y} \tag{12}$$

$$\vec{\omega}^{RI} \times {}^{R}\vec{p} = -NY\hat{x} + NX\hat{y} \tag{13}$$

$$\vec{\omega}^{RI} \times (\vec{\omega}^{RI} \times {}^{R}\vec{p}) = -N^2X\hat{x} - N^2Y\hat{y} \tag{14}$$

Substituting Eqs. (12) and (14) into Eq. (9)

$${}^{R}\ddot{\vec{p}} = -2(-N\dot{Y}\hat{x} + N\dot{X}\hat{z}) - (-N^2X\hat{x} - N^2Y\hat{y}) - \frac{Gm_1\vec{D}}{||\vec{D}||^3} - \frac{Gm_2\vec{R}}{||\vec{R}||^3} \tag{15}$$

$\vec{D}$ and $\vec{R}$ are defined as:

$$\vec{D} = (X + D_1)\hat{x} + Y\hat{y} + Z\hat{z}$$

$$\vec{R} = (X - D_2)\hat{x} + Y\hat{y} + Z\hat{z}$$

where D_1 are D_2 are defined as the distances between the barycenter and the m_1 and m_2 masses, respectively. The equations of motion of the CR3BP in the rotating reference frame are

$$\ddot{X} = 2N\dot{Y} + N^2 X - \frac{Gm_1(X + D_1)}{D^3} - \frac{Gm_2(X - D_2)}{R^3} \tag{16}$$

$$\ddot{Y} = -2N\dot{X} + N^2 Y - \frac{Gm_1 Y}{D^3} - \frac{Gm_2 Y}{R^3} \tag{17}$$

$$\ddot{Z} = -\frac{Gm_1 Z}{D^3} - \frac{Gm_2 Z}{R^3} \tag{18}$$

The EOMs are nondimensionalized to simplify the problem further. The CR3BP is nondimensionalized by choosing characteristic quantities for length, mass, and time. The characteristic length, l^*, is chosen as the distance between the two primary bodies. Since the distance between the two primaries is changing, a mean value for the distance is used. The characteristic mass, m^*, is chosen as the sum of the mass of the two primary bodies. The characteristic time is chosen such that the nondimensional time for one revolution will be 2π. The quantity μ is introduced, which is defined as $\mu = m_2/m^*$. The characteristic quantities are shown in Tables 1 and 2. Since the CR3BP is a chaotic system and sensitive to small changes, sixteen significant figures are used for characteristic quantities during computations. The original X, Y, Z, D, and R used in the dimensional EOMs will be represented by their respective lowercase letters in the nondimensional EOMs.

Table 1. Characteristic Quantities for Earth-Moon, Sun-Earth Systems

System	l^* (km)	m^* (kg)	t^*
Earth-Moon	384400	6.045825684978303e+24	4.342479844022600 days
Sun-Earth	149587457	1.988477791702254e+30	58.126336238550834 days

Table 2. μ **for Earth-Moon, Sun-Earth Systems**

System	μ
Earth-Moon	0.012150586550569
Sun-Earth	3.003486074446236e-06

The nondimensional equations of motion are shown in Eqs. (19)-(21), the derivatives shown with respect to time.

$$\ddot{x} = x + 2\dot{y} - \frac{(1-\mu)(x+\mu)}{d^3} - \frac{\mu(x-1+\mu)}{r^3} \tag{19}$$

$$\ddot{y} = y - 2\dot{x} - \frac{(1-\mu)y}{d^3} - \frac{\mu y}{r^3} \tag{20}$$

$$\ddot{z} = -\frac{(1-\mu)z}{d^3} - \frac{\mu z}{r^3} \tag{21}$$

where

$$d = \sqrt{(x+\mu)^2 + y^2 + z^2} \tag{22}$$

$$r = \sqrt{(x-1+\mu)^2 + y^2 + z^2} \tag{23}$$

The CR3BP is a highly coupled set of nonlinear ODEs. There exists no closed-form solution for the CR3BP differential equations [14]. Therefore, trajectories in the CR3BP are calculated using numerical integration.

2.3.1 Coordinate Transformations.

It is often useful to visualize trajectories in an inertial reference frame. A transformation matrix will be derived to convert from the barycentric rotating reference frame to an Earth-Centered Inertial (ECI) frame. The ECI frame is non-rotating and the origin lies at the center of the Earth. In this particular ECI frame, the z-axis will be the same as the z-axis of the barycentric rotating frame. The CR3BP rotating reference frame is centered at the m_1-m_2 barycenter. Before performing the rotation, the position in the barycentric rotating frame must be offset by μ in the x direction. After the offset is performed, the new position in the ECI frame is found with a rotation about the z-axis:

$$ {}^{I}p = \begin{bmatrix} \cos(\theta) & -\sin(\theta) & 0 \\ \sin(\theta) & \cos(\theta) & 0 \\ 0 & 0 & 1 \end{bmatrix} ({}^{R}p + \mu\hat{x}) \tag{24} $$

The angle θ represents the barycentric frame offset from the ECI frame about the z-axis. The angle θ can be given at a desired value at initial time, and is then advanced using the constant rotation of the CR3BP rotating reference frame. The R and I superscripts represent the rotating and inertial reference frames respectively, and p represents the position. To get an expression for the rotating velocity in the inertial frame, the product rule is used as outlined in [7].

$$ {}^{I}\dot{p} = \begin{bmatrix} -\sin(\theta) & -\cos(\theta) & 0 \\ \cos(\theta) & -\sin(\theta) & 0 \\ 0 & 0 & 1 \end{bmatrix} ({}^{R}p + \mu\hat{x}) + \begin{bmatrix} \cos(\theta) & -\sin(\theta) & 0 \\ \sin(\theta) & \cos(\theta) & 0 \\ 0 & 0 & 1 \end{bmatrix} {}^{R}\dot{p} \tag{25} $$

Eqs. (24) and (25) are combined to get the transformation of the full state into the inertial frame:

$$\begin{bmatrix} {}^{I}p \\ {}^{I}\dot{p} \end{bmatrix} = \begin{bmatrix} \cos(\theta) & -\sin(\theta) & 0 & 0 & 0 & 0 \\ \sin(\theta) & \cos(\theta) & 0 & 0 & 0 & 0 \\ 0 & 0 & 1 & 0 & 0 & 0 \\ -\sin(\theta) & -\cos(\theta) & 0 & \cos(\theta) & -\sin(\theta) & 0 \\ \cos(\theta) & -\sin(\theta) & 0 & \sin(\theta) & \cos(\theta) & 0 \\ 0 & 0 & 1 & 0 & 0 & 1 \end{bmatrix} \begin{bmatrix} ({}^{R}p + \mu\hat{x}) \\ {}^{R}\dot{p} \end{bmatrix} \tag{26}$$

2.3.2 Equilibrium Points.

An equilibrium point of a dynamic system is a state that does not change over time, or a fixed point. If the equations of motion for a system are known, $f(\vec{X}, t)$, the equilibrium points are solved for by finding the states $\vec{X}_e$ where the following is true:

$$f(\vec{X}_e, t) = 0 \tag{27}$$

The equilibrium points in the CR3BP are known as Lagrange points. The three collinear Lagrange points were first discovered by Leonhard Euler in 1765 [15]. The equations of motion shown in Eqs. (19)-(21) are examined to find the collinear Lagrange points. The velocity components for equilibrium points will be zero: $\dot{x} = 0,\ \dot{y} = 0,\ \dot{z} = 0$. Setting $y = 0$ and $z = 0$, acceleration is eliminated in the y and z directions. This leaves the following:

$$\ddot{x} = x - \frac{(1-\mu)(x+\mu)}{\left(\sqrt{(x+\mu)^2}\right)^3} - \frac{\mu(x-1+\mu)}{\left(\sqrt{(x-1+\mu)^2}\right)^3} \tag{28}$$

This is now a matter of finding the values of x which will satisfy $\ddot{x} = 0$. A Newton-Raphson method can be implemented to solve for the three collinear points. These are shown for the Earth-Moon system in Table 3.

Table 3. Collinear Lagrange Points in the Earth-Moon System

Lagrange Point	x (Nondimensional)	y (Nondimensional)
L_1	0.836915121142416	0
L_2	1.155682169063843	0
L_3	-1.005062646202315	0

The last two Lagrange points were discovered by Lagrange in 1772 [16], from which they get their name. These are found by setting $r = d = 1$. This satisfies zero acceleration for Eqs. (19) and (20). This leaves the equation of motion:

$$\ddot{z} = -z \tag{29}$$

which is satisfied when $z = 0$. The values of x and y which satisfy $r = 1$ and $d = 1$ are then found. There are two equations, Eqs. (22) and (23), and two unknowns x and y. Solving for x and y gives:

$$x = \frac{1}{2} - \mu \tag{30}$$

$$y = \pm\sqrt{3}/2 \tag{31}$$

The positive y corresponds to the fourth Lagrange point and the negative y to the fifth Lagrange point.

Table 4. Equilateral Lagrange Points in the Earth-Moon System

Lagrange Point	x (Nondimensional)	y (Nondimensional)
L_4	0.487849413449431	0.866025403784439
L_5	0.487849413449431	-0.866025403784439

Figure 4 shows the five Lagrange points of the Earth-Moon system in the CR3BP reference frame.

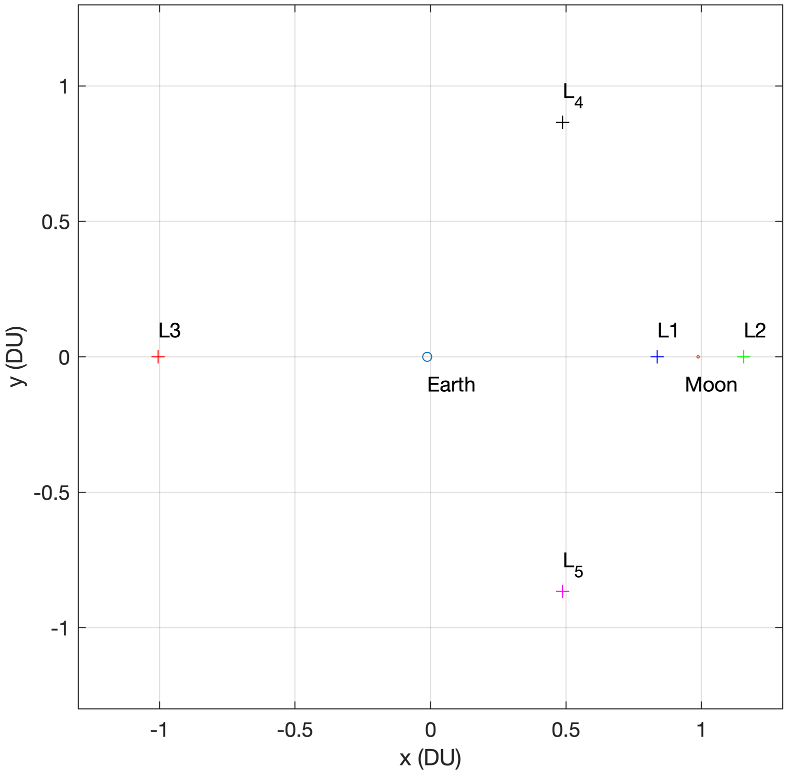

Figure 4. Lagrange Points in the Earth-Moon System

2.3.3 Jacobi's Constant.

Energy is not a constant in the CR3BP due to the rotating formulation of the differential equations [14]. However, there is an "energy-like" integral of motion, known as Jacobi's Constant (JC). Jacobi's Constant is derived in this section, starting by introducing the CR3BP pseudo-potential. The pseudo-potential function is defined as:

$$U^* = \frac{x^2 + y^2}{2} + \left(\frac{1-\mu}{d} + \frac{\mu}{r}\right) \tag{32}$$

The partial derivatives of the pseudopotential with respect to x, y, and z are

$$U^*_x = x - \frac{(1-\mu)(\mu+x)}{((x+\mu)^2 + y^2 + z^2)^{3/2}} - \frac{\mu(\mu+x-1)}{((x+\mu-1)^2 + y^2 + z^2)^{3/2}} \tag{33}$$

$$U^*_y = y - \frac{(1-\mu)y}{((x+\mu)^2 + y^2 + z^2)^{3/2}} - \frac{\mu y}{((\mu+x-1)^2 + y^2 + z^2)^{3/2}} \tag{34}$$

$$U^*_z = -\frac{(1-\mu)z}{((x+\mu)^2 + y^2 + z^2)^{3/2}} - \frac{\mu y}{((\mu+x-1)^2 + y^2 + z^2)^{3/2}} \tag{35}$$

Substituting these partial derivatives into the equations of motion gives

$$\ddot{x} - 2\dot{y} = U^*_x \tag{36}$$

$$\ddot{y} + 2\dot{x} = U^*_y \tag{37}$$

$$\ddot{z} = U^*_z \tag{38}$$

Next, multiplying Eq. (36) by $\dot{x}$, Eq. (37) by $\dot{y}$, and Eq. (21) by $\dot{z}$:

$$\ddot{x}\dot{x} - 2\dot{y}\dot{x} = U^*_x\dot{x} \tag{39}$$

$$\ddot{y}\dot{y} + 2\dot{x}\dot{y} = U^*_y\dot{y} \tag{40}$$

$$\ddot{z}\dot{z} = U^*_z\dot{z} \tag{41}$$

And then adding Eqs. (39), (40), and (41), which becomes

$$\ddot{x}\dot{x} + \ddot{y}\dot{y} + \ddot{z}\dot{z} = U_x^*\dot{x} + U_y^*\dot{y} + U_z^*\dot{z} \tag{42}$$

The above on each side is the time derivatives of two quantities.

$$\frac{1}{2}\frac{d}{dt}(\dot{x}^2 + \dot{y}^2 + \dot{z}^2) = \frac{dU^*}{dt} \tag{43}$$

Now taking the integral of Eq. (43) with respect to time

$$\dot{x}^2 + \dot{y}^2 + \dot{z}^2 = 2U^* - C \tag{44}$$

where C is a constant of integration. Rearranging arrives at the definition of Jacobi's Constant in Eq. (45), where v is the absolute value of the velocity.

$$C = 2U^* - v^2 \tag{45}$$

The change in the Jacobi Constant can be tracked during numerical integration. Being a constant, the Jacobi Constant should only be expected to change near the same order of magnitude as the integration tolerances.

2.3.4 Zero-Velocity Curves.

The Jacobi Constant can provide insight into permissible and forbidden regions in the CR3BP without changes to the JC. The zero-velocity curves (ZVC) are the locus of points that satisfy zero velocity in the rotating frame for a given JC [11]. The curve represents the bounded region where a spacecraft can travel, and areas outside of the ZVC are considered the forbidden region. This is because a satellite in a forbidden region for a specific JC would require a complex velocity. Plotting the ZVC tells us where a satellite can travel without performing a ΔV. The interior region, exterior region, and Moon region are only accessible for certain energy levels [17].

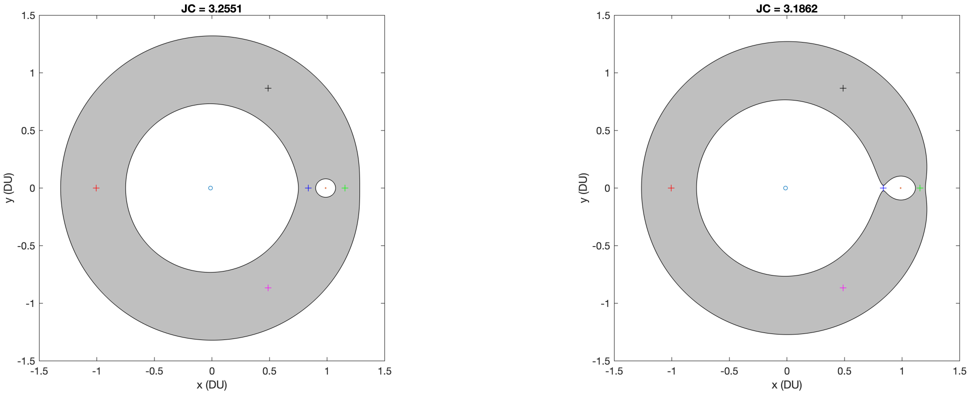

(a) JC = 3.2551

(b) JC = 3.1862

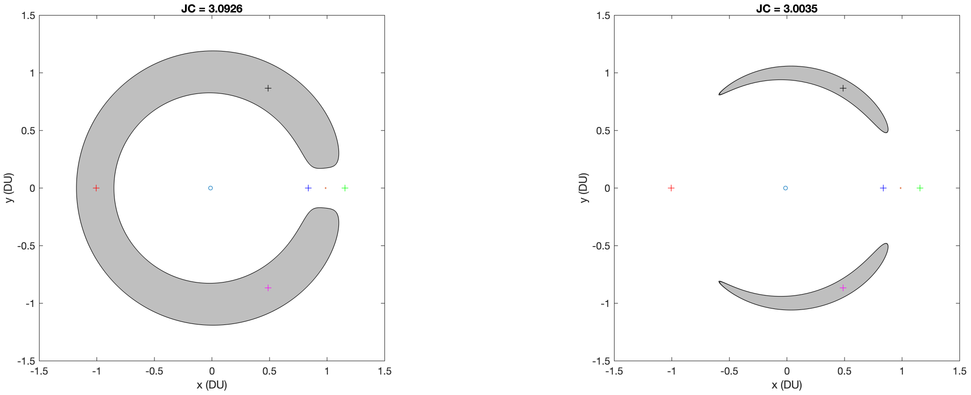

(c) JC=3.0962

(d) JC=3.0035

Figure 5. Forbidden Regions for Varying Jacobi Constants, Forbidden Regions Drawn in Gray

As shown in Figures 5a-5d, the forbidden region can restrict a satellite from moving between the different regions. In Figure 5a, all three regions are restricted from reaching the others. In Figure 5b, the interior region is able to reach the Moon region. In Figure 5c the interior, exterior, and Moon regions are all accessible to eachother.

2.3.5 State Transition Matrix.

The state transition matrix (STM) is used to understand the trajectories "close" to a given numerically integrated trajectory [18], shown in Eq. (46). The STM provides the understanding of "close" trajectories by giving information about the sensitivity of the final state to initial conditions, and is also known as the sensitivity matrix. The STM satisfies the differential equation shown in Eq. (47) [18].

$$\Phi(t, t_0) = \frac{\partial \mathbf{X}(t)}{\partial \mathbf{X}(t_0)} \tag{46}$$

$$\dot{\Phi}(t, t_0) = A(t)\Phi(t, t_0) \tag{47}$$

$$\Phi(t_0, t_0) = I \tag{48}$$

The matrix $A(t)$ is the first order partial derivative of the equations of motion with respect to the problem variables, shown in Eq. (49).

$$A(t) = \frac{\partial \boldsymbol{f}}{\partial \mathbf{X}} \tag{49}$$

For the planar CR3BP, A(t) is shown in Eq. (50). The pseudopotential U^* is shown in Eq. (32).

$$A(t) = \begin{bmatrix} 0 & 0 & 1 & 0 \\ 0 & 0 & 0 & 1 \\ U^*_{xx} & U^*_{xy} & 0 & 2 \\ U^*_{yx} & U^*_{yy} & -2 & 0 \end{bmatrix} \tag{50}$$

For the planar CR3BP, Φ is defined in Eq. (51).

$$\Phi(t, t_0) = \begin{bmatrix} \frac{\partial x(t)}{\partial x(t_0)} & \frac{\partial x(t)}{\partial y(t_0)} & \frac{\partial x(t)}{\partial \dot{x}(t_0)} & \frac{\partial x(t)}{\partial \dot{y}(t_0)} \\ \frac{\partial y(t)}{\partial x(t_0)} & \frac{\partial y(t)}{\partial y(t_0)} & \frac{\partial y(t)}{\partial \dot{x}(t_0)} & \frac{\partial y(t)}{\partial \dot{y}(t_0)} \\ \frac{\partial \dot{x}(t)}{\partial x(t_0)} & \frac{\partial \dot{x}(t)}{\partial y(t_0)} & \frac{\partial \dot{x}(t)}{\partial \dot{x}(t_0)} & \frac{\partial \dot{x}(t)}{\partial \dot{y}(t_0)} \\ \frac{\partial \dot{y}(t)}{\partial x(t_0)} & \frac{\partial \dot{y}(t)}{\partial y(t_0)} & \frac{\partial \dot{y}(t)}{\partial \dot{x}(t_0)} & \frac{\partial \dot{y}(t)}{\partial \dot{y}(t_0)} \end{bmatrix} \tag{51}$$

Numerically integrating the Φ matrix (Eq. (51)) and the N equations of motion (Eqs. (19)-(21)) requires simultaneously calculating $N^2 + N$ first order differential equations. The N corresponds to the equations of motion, and N^2 corresponds to the Φ matrix. For the planar CR3BP, N=4, and 20 first order differential equations must be numerically integrated. This is more computationally expensive than the four equations of motion needed to numerically integrate a trajectory. The STM will be used to target periodic orbits in the CR3BP as shown in Section 2.3.6, and to find stable and unstable manifolds as shown in Section 2.4.

2.3.6 Lyapunov Orbits.

One symmetry in the planar CR3BP is over the x axis and time, such that if $x = x(t)$, $y = y(t)$ is a solution, then $x = x(-t)$, $y = -y(-t)$ is also a solution [13]. If a trajectory has two perpendicular crossing of the x-axis, then its mirrored trajectory across the x-axis will also have two perpendicular crossings, and will effectively "close the loop" and is a periodic orbit in the CR3BP reference frame. The periodic orbits that orbit a Lagrangian point and lie in the $x-y$ plane are known as Lyapunov orbits.

In order to find Lyapunov orbit solutions the shooting method is used. The shooting method is a multi-dimensional version of Newton's method [18]. Newton's method seeks to find roots of real-value functions. The STM is numerically integrated while implementing the shooting method and supplies the gradient information required

[14]. In the Newton formulation, the design variables are designated as the vector $\mathbf{X}$ [14].

$$\mathbf{X} = \begin{bmatrix} X_1 \\ \vdots \\ X_n \end{bmatrix} \tag{52}$$

The shooting method is performed to achieve some conditions, defined by constraint equations $F(X)$, shown in Eq. (53). The constraint equations might be to satisfy a final position or velocity, angle of attack, altitude, etc.

$$\mathbf{F}(\mathbf{X}) = \begin{bmatrix} F_1(\mathbf{X}) \\ \vdots \\ F_m(\mathbf{X}) \end{bmatrix} \tag{53}$$

The Jacobian matrix, $D\mathbf{F}(\mathbf{X})$ represents the partial derivatives of the constraints with respect to the free variables [14]:

$$D\mathbf{F}(\mathbf{X}) = \frac{\partial \mathbf{F}}{\partial \mathbf{X}} = \begin{bmatrix} \frac{\partial F_1}{\partial X_1} & \frac{\partial F_1}{\partial X_2} & \cdots & \frac{\partial F_1}{\partial X_n} \\ \frac{\partial F_2}{\partial X_1} & \frac{\partial F_2}{\partial X_2} & \cdots & \frac{\partial F_2}{\partial X_n} \\ \vdots & \vdots & \ddots & \\ \frac{\partial F_m}{\partial X_1} & \frac{\partial F_m}{\partial X_2} & & \frac{\partial F_m}{\partial X_n} \end{bmatrix} \tag{54}$$

The update equation for the shooting method is defined as Eq. (55).

$$\mathbf{X}^{j+1} = \mathbf{X}^j - D\mathbf{F}(\mathbf{X}^j)^{-1}\mathbf{F}(\mathbf{X}^j) \tag{55}$$

In Eq. (55), $\mathbf{X}^{j+1}$ represents the next iteration. The shooting method continues to iterate until an error tolerance between the final conditions to the target conditions is met.

In the case of targeting an L_1 Lyapunov orbit, the goal is to find a trajectory with two perpendicular crossings of the x-axis. The initial state will be along the x-axis with no x component of velocity. The target state will also be on the x-axis with no x component of velocity. The control variables are then time of flight and the initial y component of velocity

$$\mathbf{X} = \begin{bmatrix} \dot{y}_0 \\ t_f \end{bmatrix} \tag{56}$$

The contraint equations are constructed such that final y position is zero, and the final x velocity is zero.

$$\mathbf{F}(\mathbf{X}) = \begin{bmatrix} y_t - y_f \\ \dot{x}_t - \dot{x}_f \end{bmatrix} = \begin{bmatrix} 0 \\ 0 \end{bmatrix} \tag{57}$$

The t subscript denotes target (in this case both y_t and $\dot{x}_t$ are 0) and f denotes final time in Eq. (57). The Jacobian matrix $D\mathbf{F}(\mathbf{X})$ is defined as Eq. (58).

$$D\mathbf{F}(\mathbf{X}) = \begin{bmatrix} \frac{\partial y_f}{\partial \dot{y}_0} & \frac{\partial y_f}{\partial t} \\ \frac{\partial \dot{x}_f}{\partial \dot{y}_0} & \frac{\partial \dot{x}_f}{\partial t} \end{bmatrix} = \begin{bmatrix} \frac{\partial y_f}{\partial \dot{y}_0} & \dot{y}_f \\ \frac{\partial \dot{x}_f}{\partial \dot{y}_0} & \ddot{x}_f \end{bmatrix} \tag{58}$$

Information from the STM and the state from final time are used to define the Jacobian matrix. The shooting method requires an initial guess, and if a poor initial guess is chosen then the shooting method may not converge, or may take a long time to converge. Using a method like Lambert's problem might be a good enough initial guess in some cases. In this case the initial state of a periodic orbit in the linearized system was used as an initial guess [13]. The shooting method being used to target a perpendicular crossing of the x-axis is shown in Figure 6.

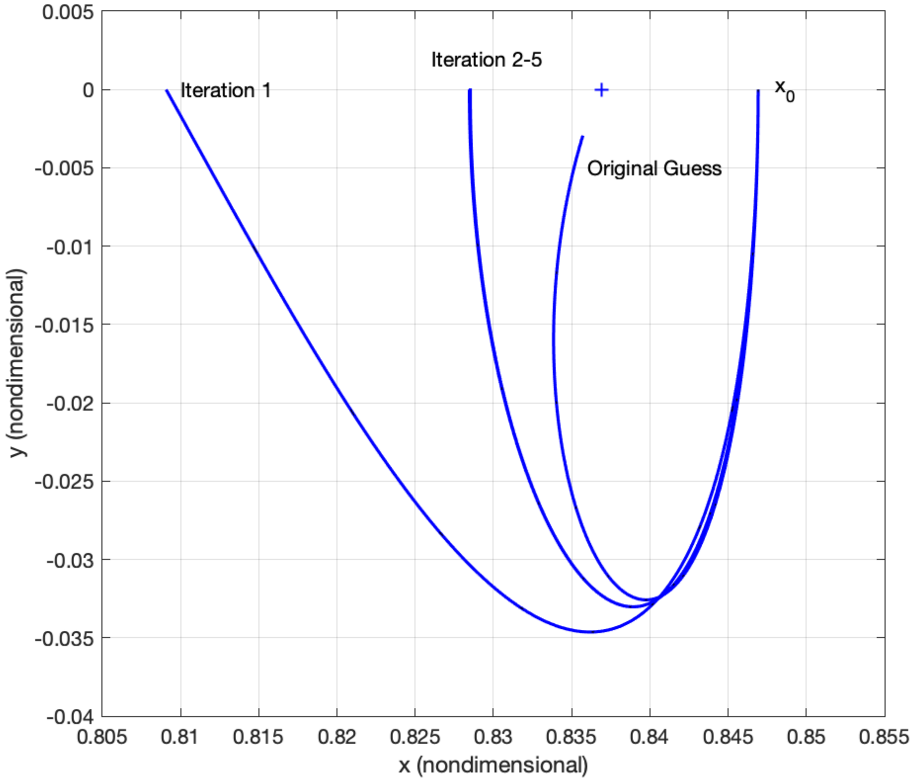

Figure 6. Shooting Method Targeting Perpendicular Crossing of x-axis

Additional periodic orbits can be found using numerical continuation [19]. This numerical continuation takes a known periodic orbit with the state on the x-axis, and displaces the x position by some amount. This displaced state is used as the initial guess for finding a new periodic orbit. The ΔX must be small enough for the shooting method to converge. Continuation is often used to generate families of periodic orbits around Lagrange points [19]. A family of periodic orbits around the L_1 Lagrange point is shown in Figure 7.

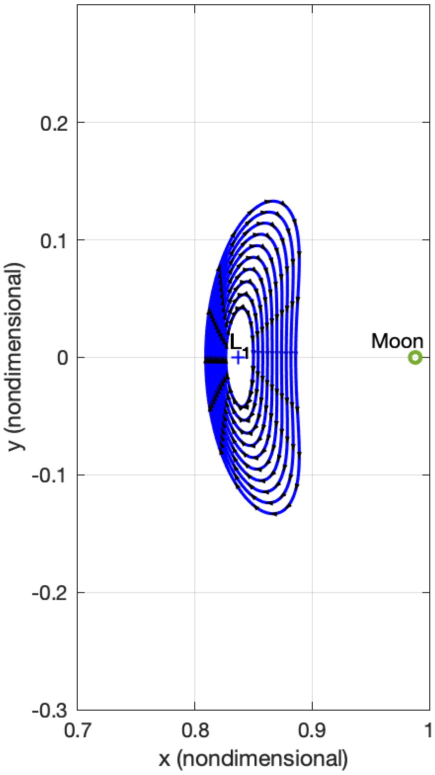

Figure 7. L_1 **Lyapunov Orbits Found Using Continuation Method**

2.4 Stable and Unstable Manifolds

Manifolds are defined as "surfaces of lower dimension embedded within the phase space"[18]. This is also to say that, in the CR3BP model, once a trajectory is on the surface of a manifold it will remain on the manifold [20]. The path of the orbits in the manifold constitute the surface of the manifold. Also considered manifolds are trajectories that asymptotically approach and leave the manifolds, which are called stable and unstable manifolds, respectively [20]. These manifolds are also titled invariant manifolds, and have origins rooted in dynamical systems theory.

Stable and unstable manifolds have been described as "low energy passageways" for their ability to connect separate regions of the CR3BP [19]. This is true of the stable and unstable manifolds associated with periodic orbits around L_1 and L_2, which are able to transport objects between the two primary bodies [19]. Using stable and unstable manifolds has shown to be useful in trajectory design, where conventional tools fall short of understanding the multi-body problem [20]. These manifolds serve as a guide to understanding the dynamical flow of the CR3BP, and offer design options for targeting orbits around Lagrange points [20].

In order to find the stable and unstable manifolds from a periodic orbit, information about the trajectories near the periodic orbit is required, and the STM is used [19]. Specifically, the monodromy matrix is used, which is the STM after one complete orbit. The eigenvalues of the monodromy matrix will reveal the stability of the periodic orbit. In the case of Lyapunov orbits in the planar CR3BP, the following eigenvalues will exist [19]

$$\lambda_1 > 1; \ \lambda_2 = \frac{1}{\lambda_1}; \ \lambda_3 = \lambda_4 = 1 \tag{59}$$

The eigenvalue greater than one corresponds to an unstable eigenvector, v^u, and the eigenvalue less than one corresponds to a stable eigenvector, v^s. Suppose the state $\vec{x}_0$ is the starting point from which the monodromy matrix, $\Phi(0, T)$, was calculated. One period of the orbit is T. To move the state onto the unstable or stable manifold requires the perturbations shown in Eq. (60) and (61), respectively.

$$\vec{x}^u = \vec{x}_0 + \epsilon v^u \tag{60}$$

$$\vec{x}^s = \vec{x}_0 + \epsilon v^s \tag{61}$$

In Eqs. (60) and (61), ϵ should be sufficiently small so as not to violate the linear estimate, but not too small such that the time of flight to depart or approach the periodic orbit is too long [19]. When multiple stable and unstable manifolds are propagated they form manifold tubes as they travel throughout different regions of the CR3BP. In order to see the motion of these tubes unstable manifolds are propagated in positive time, and stable manifolds are propagated in negative time. Stable and unstable manifold tubes from L_1 and L_2 Lyapunov orbits are shown in Figures 8 and 9.

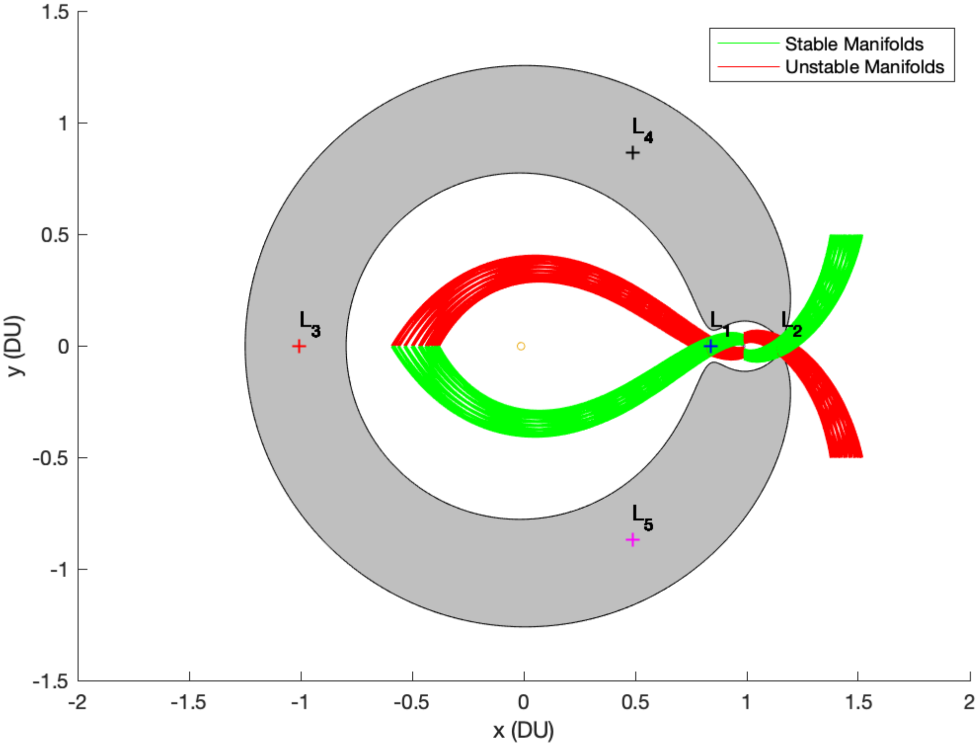

Figure 8. L_1 and L_2 Lyapunov Orbit Manifold Tubes

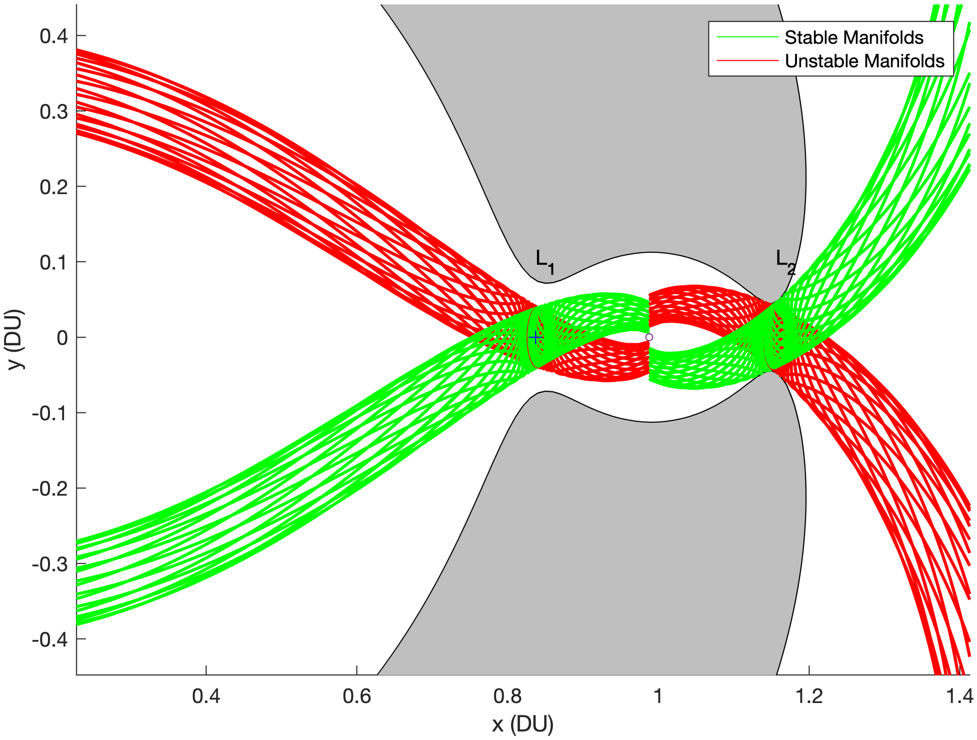

Figure 9. L_1 **and** L_2 **Lyapunov Orbit Manifold Tubes**

2.5 Genetic Algorithms

Genetic algorithms (GA) are a stochastic optimization method which attempt to mimic principles of Darwinian evolution [21]. A group of possible solutions called individuals make up a generation. Each individual in the generation is evaluated, and then acted upon by genetic operators to search for better solutions. Genetic algorithms use three basic operators: selection, crossover, and mutation. Selection is the process of choosing which individuals will move on to create the next generation, which is done through the evaluation of a fitness function. Crossover is the process of producing a child solution from more than one parent solution. Mutation is the process of randomly changing characteristics of an individual.

GAs offer a number of advantages over other methods. GAs require no initial guess to start the optimization process. The initial population is randomly generated, although initial population guesses can also be provided. They are also more likely in general to find a global minima than other methods which may converge onto local minima [11]. GAs are robust, and are easily implemented without requiring a detailed understanding of the optimization problem [22]. A drawback to GAs is they are computationally expensive compared to other optimization techniques that leverage gradient information [21]. This is especially true when constraints are imposed on the problem.

2.6 Trajectory Optimization

Most common trajectory optimization methods can fit into two categories: direct and indirect [22]. Indirect methods require deriving necessary conditions for optimality [23], while direct methods typically transcribe the problem into a nonlinear programming problem. Both methods provide benefits and drawbacks. Indirect methods have a small region of convergence and require an initial guess fairly close to the optimal solution, where direct methods tend to have a more robust convergence [22]. Indirect methods are more difficult to implement because they require analytically deriving conditions for optimality, which can be complex for nonlinear dynamics and constraints [22]. For these reasons, indirect methods have become increasingly less common in space trajectory optimization [11].

Another distinguisher between trajectory optimization problems is the use of impulsive-thrust or continuous-thrust. Impulsive-thrust assumes that a change in velocity is preformed instantaneously. Impulsive-thrust maneuvers become parameter optimization problems, which tend to be solved directly, with parameters like magnitude of ΔV, direction, and timing [11]. Continuous-thrust, however, requires solving for control variables with continuous time histories [11]. This study is concerned with impulsive-thrust maneuvers, and the continuous-thrust case will not be considered.

The parameter optimization problem of impulsive-thrust trajectory optimization lends itself to be solved using nonlinear programming (NLP). NLP has become an indispensable tool for trajectory optimization, which uses gradient information to converge to local minima while satisfying constraints [23]. There are a vast number of NLP solvers in use, one in particular is MATLAB's *fmincon().* The NLP solver *fmincon()* is a multi-purpose parameter optimizer that has been used for a wide number of spacecraft trajectory optimization problems [23]. In this study *fmincon()* will be solving two-point boundary value problems (TPBVP) (that is, solving for the trajectory between two stationary positions in the CR3BP) using sequential quadratic programming (SQP) to solve the nonlinear optimization problem. A significant drawback to the NLP solver is its likelihood to converge onto a solution in the neighborhood of the initial guess [11]. This is especially challenging for a multimodal design space where many local minima exist [21]. Evolutionary algorithms, and in specific genetic algorithms, may be more suited to search these design spaces to find global minima. However, genetic algorithms also have significant drawbacks. Hybrid techniques combining genetic algorithms and gradient-based methods have been shown to be effective for a number of trajectory design applications [24] [25] [21]. These hybrid techniques have also been termed as memetic algorithms (MA) [26]. Memetic algorithms are a population based search where the individuals are able to search for local minima [26]. The relation to Darwinian evolution is the ability of an individual to adapt and learn during its lifetime given some baseline characteristics (genes).

Cislunar trajectory optimization has been a renewed topic with the growing interest in sending missions to the Moon. In combination with this renewed interest are the advancements in dynamical systems theory (DST) and the proven effectiveness of invariant manifolds in mission design [9] [27]. Invariant manifolds in the CR3BP open up new pathways to travel to and from the libration points [20] which offer new low-fuel trajectories [11]. Stable manifolds can now be used as patch points instead of the periodic orbits from which they originate [20]. Similarly, unstable manifolds can be traveled departing a periodic orbit until a suitable patch point is found. What is left is a TPBVP to be solved between a point on the manifold and the start/ending orbit [11].

The optimization technique in this study will leverage the global search ability of genetic algorithms. The technique will also use the quick convergence of NLP solvers and their ability to handle complex constraints by using gradient information. Finally, this study will use invariant manifolds to leverage the natural dynamics of the CR3BP.

2.7 Summary

This chapter defined the CR3BP and its characteristics, including stable and unstable manifolds, Lagrange points, and periodic orbits around Lagrange points. The CR3BP will be the model used for the test cases in Chapter 3. This chapter also gave a brief overview of trajectory optimization techniques. Chapter 3 will describe the genetic algorithm–direct method hybridization technique that will be used in this research to solve for optimal transfers in the CR3BP. The hybridization technique will also incorporate CR3BP manifolds and periodic orbits as have been discussed in this chapter.

III. Research Methodology

3.1 Chapter Overview

This chapter will outline the research methodology which will be used to answer the research questions listed in Chapter 1. The test plans will include finding transfers from L_1 and L_2 Lyapunov orbits to GEO. The details of the test plans will be given. This chapter will also describe the hybridization technique that is used to solve for the transfers.

3.2 Problem Description

The planar CR3BP is considered in this thesis. Because the Moon's orbit is inclined with respect to the Earth's equatorial plane, the target orbit is geosynchronous but not geostationary, where most satellites in GEO reside. The dimensions of the two Lyapunov orbits are given in Table 5 and shown in Figure 10.

Table 5. L_1 and L_2 Lyapunov Orbit Details

Orbit	x (km)	y (km)	JC
L_1	28,024.6	95,168.4	3.126294272311462
L_2	36,656.8	101,734.0	3.126294272311462

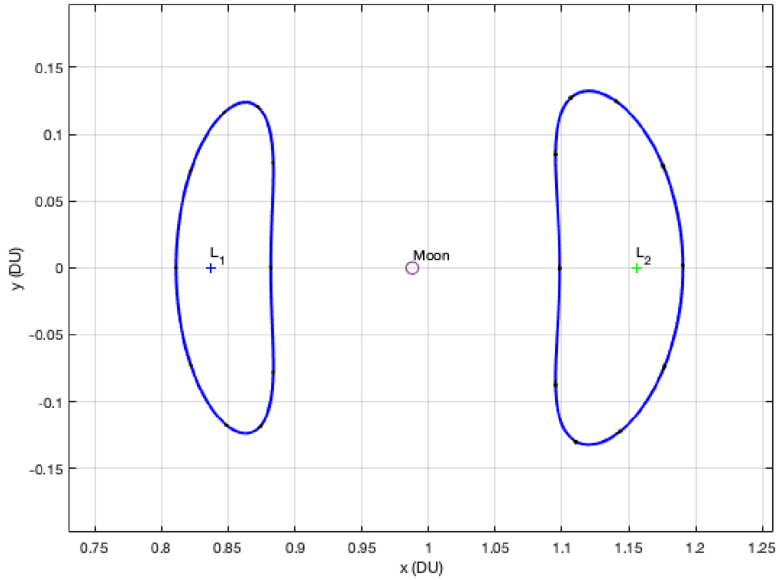

Figure 10. L_1 **and** L_2 **Lyapunov Orbits Used in Tests**

3.2.1 Sun-Exclusion Zone.

Traditionally, ground based radars have been used to track objects in low Earth orbit, while objects in higher orbits (such as geosynchronous) have been tracked using optical systems [30]. The Space-Based Visible (SBV) program is an example of space-based space surveillance, and relied on a visible band electro-optical camera [31]. Visible sensors, like the one used in the SBV program, are limited to detecting targets illuminated by the Sun [31]. Ground-based optical sensors are larger and more sensitive to light, but are also limited by the weather and tend to operate only at night [30]. Both ground- and space-based optical sensors are limited in detecting objects when they pass between the Earth and the Sun, or the Sun-exclusion zone. In order for an optical sensor to detect light reflected from a target, the object must remain outside of the SEZ. The SEZ will be defined as the angle between the Sun and the target as viewed from the center of the Earth, which will be assumed to be 50 degrees [30] [6], shown in Figure 11.

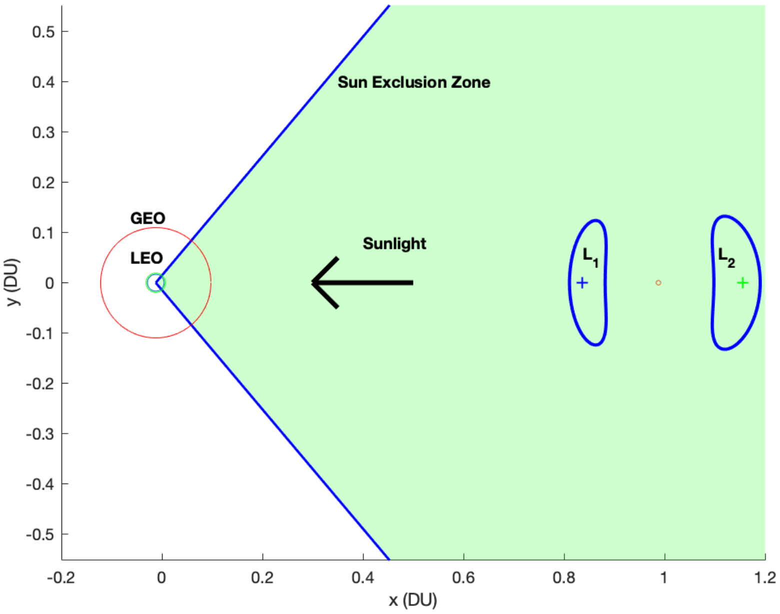

Figure 11. Sun-Exclusion Zone

In Tests 2-5 the objective for the satellite will be to arrive at geosynchronous orbit while remaining in the Sun-exclusion zone of an optical sensor that is located at Earth. Remaining in the SEZ would make the satellite unobservable to the optical sensor of interest. If an optical sensor's field of view is pointed in the direction of a spacecraft while it lies in the Sun-exclusion zone, the optical sensor cannot detect that satellite. Therefore, the search technique of the optical sensor does not need to be considered.

A fundamental assumption of the CR3BP is that the two major bodies are rotating about the common barycenter at a constant angular rate ${}^{I}\vec{\omega}_{Earth-Moon}$, where I represents an inertial reference frame. In order to include a Sun vector, the rotation of the Sun-Earth system needs to be incorporated to know the pointing of the Sun vector. For this purpose, it will also be assumed that the Sun and Earth are rotating at a constant angular rate about their common barycenter, ${}^{I}\vec{\omega}_{Sun-Earth}$.

The Sun vector can be tracked by initializing the vector and tracking its rotation using the angular rate of the Sun-Earth system in the Earth-Moon CR3BP reference frame. The initialization of the Sun-Vector angle can be chosen at different values at t_0 to examine different scenarios. The Sun-Earth and the Earth-Moon orbits are assumed to be in the same plane for all of the tests. In order to examine additional seasonal variations, the plane differences between the orbits would need to be considered.

3.3 GA–Direct Method Hybridization

Hybrid optimization techniques have been shown to be effective in the design of interplanetary missions. Because interplanetary missions are expansive and multimodal, genetic algorithms are used for their global search ability [21]. Genetic algorithms have shown to be useful when paired with patched-conic mission analysis code for inerplanetary trajectory optimization [28].

The hybrid framework has also been applied to the CR3BP. The hybrid technique has been used to design transfers from low-Earth orbit to L_1 and L_2 Lyapunov orbits [25], and extended to include resonant orbits in the CR3BP [29]. References [25] and [29] use outer loops consisting of genetic algorithms (Non-Dominated Sorting Genetic Algorithm II [NSGA-II]) controlling phase variables, and an inner loop that uses a solver for large scale nonlinear optimization problems (Sparse Nonlinear OPTimizer [SNOPT]) to solve a boundary value problem of two points in the CR3BP.

In order to find solutions for a transfer from a given Lyapunov orbit to geosynchronous orbit a hybrid technique is used that leverages unstable manifolds in the CR3BP. This will combine a genetic algorithm to perform a global search of the design space, and a gradient-based solver to solve for a locally optimal trajectory between two boundary points. The outer loop uses MATLAB's *gamultiobj()* and controls the phase level variables. Within the genetic algorithm evaluation, *fmincon()* is used to solve a two point boundary value problem. This will be a multi-objective optimization problem, where time of flight and ΔV will be optimized simultaneously to find the Pareto optimal solutions.

3.4 Test Plan Overview

The objective of the following tests is to examine how practical it is for a satellite to transfer to geosynchronous orbit from L_1 and L_2 Lyapunov orbits and remain in the Sun-exclusion zone. In order to assess the feasibility of such transfers the Pareto optimal solutions are solved for to provide a trade space for decision makers and mission planners. These solutions are found using a hybrid framework optimizing time of flight and total ΔV.

In order to establish the feasibility of the transfer from L_1 and L_2 to GEO with SEZ constraints, the Pareto front will first be found without any SEZ constraints (Test 1). This will serve as a baseline for when SEZ constraints are imposed in Tests 2-5. The objectives will be the TOF to reach geosynchronous orbit from the starting orbits, and the ΔV required in the impulsive maneuvers. The starting orbits will be Lyapunov orbits around L_1 and L_2 with matching Jacobi Constants.

In Tests 2-5 the transfer will be constrained to remain in the SEZ, and the Pareto fronts solved for. These Pareto fronts will be compared to the baseline Pareto fronts from Test 1.

In Tests 6 and 7 a limited detection range of the optical sensor will be introduced. The transfers will then be constrained to be in the SEZ, or outside of the maximum detection range during the transfer. Pareto fronts will be solved for and compared to the other tests.

Table 6. Test Plan

Test	**SEZ Constraint**	Sensor Detection Range
1	None	N/A
2	$\leq$ 10 hours outside SEZ	infinite
3	$\leq$ 3 hours outside SEZ	infinite
4	$\leq$ 1 hours outside SEZ	infinite
5	0 hours outside SEZ	infinite
6	0 hours outside SEZ while inside detection range	varies
7	0 hours outside SEZ while inside detection range	varies

3.5 Dual-Loop Framework

The following section will describe the hybridization technique between the genetic algorithm and direct method. Figure 12 shows how information is passed between *gamultiobj()* and *fmincon()* to solve for the Pareto optimal solutions. Algorithm 1 additionally shows how the genetic algorithm and direct method interact.

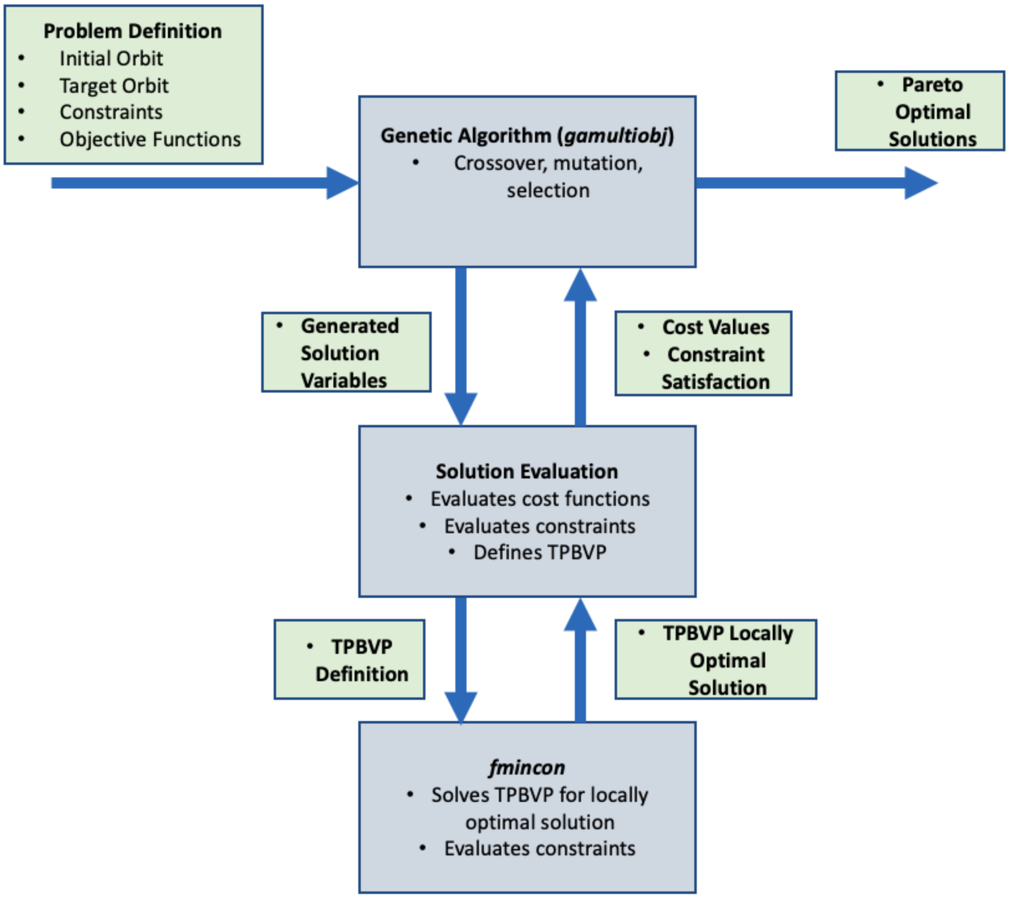

Figure 12. Hybridization Framework Overview

Algorithm 1 Hybridization Framework

```
Given: Initial and Final Orbits, Sun Constraints, $maxGenerations$
Genetic algorithm $gamultiobj()$ generates individuals $i$ in generation $G_1$
while $n$ $Generation \leq maxGenerations$ do
    for all $i$ in $G_n$ do
        Evaluate fitness and constraint satisfaction of each individual $i$.
        $fmincon()$ solves two point boundary value problem
    end for
    Genetic algorithm creates $G_{n+1}$ with selection, crossover, mutation.
end while
Pareto optimal solutions output from $G_{maxGenerations}$.
```

3.5.1 Genetic Algorithm Outer Loop.

As mentioned, *gamultiobj()* is used as the outer loop. Genetic algorithms offer a number of advantages over other methods. Genetic algorithms are more likely to find a globally optimal solution over gradient-based solvers which find locally optimal solutions [11]. Genetic algorithms do not require an initial guess to converge to a solution, whereas gradient-based solvers typically require an initial guess close enough to a minimum in order to converge [11]. Genetic algorithms are also extremely simple to implement and do not require the designer to have an in-depth knowledge of the problem being optimized [11] [22]. Genetic algorithms are a biologically inspired stochastic method and require more computation compared to methods leveraging gradient information [22].

Genetic Algorithm Variables.

Listed in Table 7 are the variables used in the genetic algorithm. A complete set of these variables would constitute a possible solution, and would be one individual of a generation.

Table 7. Variables Used in Genetic Algorithm Outer Loop

Variable	Definition	Lower Bound	Upper Bound
t_1	Length of Time in Lyapunov Orbit	0 (nondim time)	1 Period of Lyapunov Orbit
t_2	Length of Time on Unstable Manifold	0 (nondim time)	8 (nondim time)
θ	Angle to Insert Into Geosynchronous Orbit	0 radians	2π radians
$\Delta V_{perturb}$	Velocity Change to Perturb Onto Unstable Manifold	0 m/s	200 m/s
α	Objective Weighting Used for TPBVP (inner loop)	0	1
ϕ	Initial Sun Angle at $t = t_1$	0 radians	2π radians

Referencing the variables in Table 7, t_1 is the length of nondimensional time that the satellite will be in the L_1 or L_2 Lyapunov orbit before perturbing onto the unstable manifold, and is drawn in black in Figure 13. Shown in Table 7, t_2 is the length of time the satellite will coast along the unstable manifold, and is drawn in blue in Figures 13 and 14. Also in Table 7, θ represents where in geosynchronous orbit the satellite will inject into, which is shown in Figure 14. The trajectory shown in green in Figure 14 is solved for using *fmincon()*. The two boundary points are defined by the variables generated by the GA.

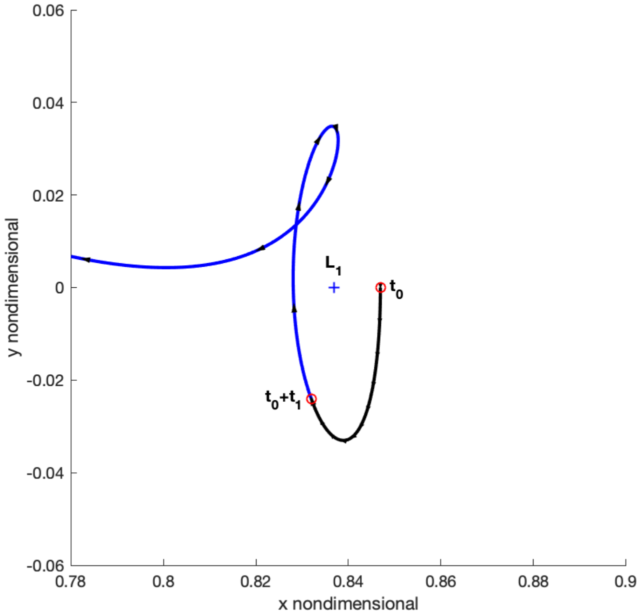

Figure 13. Sample Departure of Lyapunov Orbit

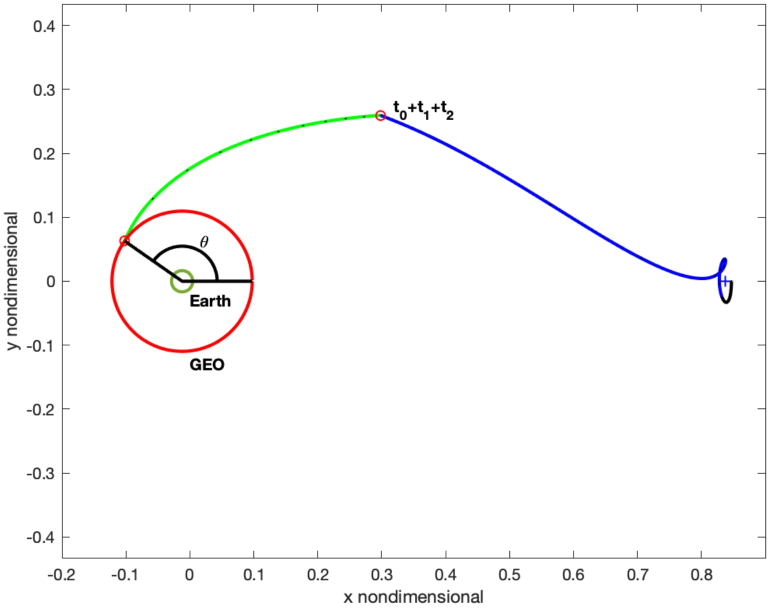

Figure 14. Sample Solution, t_1 **= 1 (nondim),** t_2 **= 3 (nondim),** $\theta = 145\ deg$, $\Delta V_{perturb} = 50\ m/s$

Genetic Algorithm Optimization Formulation.

The two objectives are to minimize time of flight and total ΔV. The MATLAB function *gamultiobj()* accepts multiple objective functions to minimize. The objective functions are shown in Eqs. (62) and (63), where $\boldsymbol{X}$ represents the control variables from Table 7.

$$J_1(\boldsymbol{X}) = t_f \tag{62}$$

$$J_2(\boldsymbol{X}) = \Delta V \tag{63}$$

The objective function $J_1(\boldsymbol{X})$ is the time spent during the transfer, from Lyapunov orbit to GEO, the components shown in Table 8. The objective function $J_2(\boldsymbol{X})$ is the sum of the three impulsive burns performed during the transfer, shown in Table 9.

Table 8. $J_1(\boldsymbol{X})$ Objective Function Components

t_2	Time in Unstable Manifold
$t_{Manifold-GEO}$	Time from the Manifold to GEO

Table 9. $J_2(\boldsymbol{X})$ Objective Function Components

$\lvert\Delta V_1\rvert$	Perturbing onto Unstable Manifold
$\lvert\Delta V_2\rvert$	Maneuvering off Unstable Manifold
$\lvert\Delta V_3\rvert$	Inserting into GEO

$$J_1 = t_2 + t_{Manifold-GEO}$$

$$J_2 = |\Delta V_1| + |\Delta V_2| + |\Delta V_3|$$

The variables t_2 and $|\Delta V_1|$ come from the genetic algorithm outer loop variables shown in Table 7. The variables $t_{Manifold-GEO}$, ΔV_2, and ΔV_3 are solved for in the inner loop shown in Section 3.5.2. The inner loop uses *fmincon()* to solve a TPBVP from the unstable manifold to the injection point in GEO.

For Test 1 there are no equality constraints, inequality constraints, linear inequalities, or linear equailities included in the outer loop optimization formulation:

$$\begin{aligned} \underset{\boldsymbol{X}}{\text{minimize}} \quad & J_1(\boldsymbol{X}), J_2(\boldsymbol{X}) \\ \text{subject to} \quad & \dot{\mathbf{x}} = \mathbf{f}(t, \mathbf{x}) \end{aligned} \tag{64}$$

The equations of motion, $\dot{\mathbf{x}} = \mathbf{f}(t, \mathbf{x})$, are defined in Eqs. (19)-(21). When a keep out zone is enforced in Tests 2-7, there will be an inequality constraint that the time spent in the keep-out zone is less than the time allowed in the keep out zone:

$$\begin{aligned} \underset{\boldsymbol{X}}{\text{minimize}} \quad & J_1(\boldsymbol{X}), J_2(\boldsymbol{X}) \\ \text{subject to} \quad & \dot{\mathbf{x}} = \mathbf{f}(t, \mathbf{x}), \\ & c(\boldsymbol{X}) = t_{KOZ} - t_{allowed-KOZ} \leq 0 \end{aligned} \tag{65}$$

This optimization formulation does not include a constraint that the final position be the desired position in GEO. This is because the final position constraint is handled within the inner loop, which will be described in Section 3.5.2.

3.5.2 Direct Method Inner Loop.

The inner loop solves the two point boundary value problem which is defined by the outer loop. MATLAB's *fmincon()* is used. A sufficiently close initial guess is required for *fmincon()* to converge to a feasible solution. Lambert's problem is used as an initial guess [32].

Direct Method Optimization Formulation.

The inner loop finds the locally optimal solution to a TPBVP. The NLP solver *fmincon()* chooses the variables $\boldsymbol{X}$ to minimize the scalar function $J(\boldsymbol{X})$ subject to constraints.

The variables in $\boldsymbol{X}$ are the initial changes in x and y velocity at initial time, and the time of flight, shown in Eq. (66). The two boundary points for the TPBVP are the end of the unstable manifold and the injection point into GEO.

$$\boldsymbol{X} = \begin{bmatrix} \Delta V_{x0} \\ \Delta V_{y0} \\ t_f \end{bmatrix} \tag{66}$$

The velocity in Eq. (66) make up the components of $|\Delta V_2|$ from Table 9. The objective function $J(\boldsymbol{X})$ is defined by the time of flight and total ΔV shown in Eq. (67). The variable α is defined by the genetic algorithm from Table 7.

$$J(\boldsymbol{X}) = \alpha \Delta V + (1 - \alpha) t_f \tag{67}$$

The ΔV in Eq. (67) corresponds to the summation of $|\Delta V_1|$ and $|\Delta V_2|$ from Table 9. Equality constraints are imposed such that the final position is the desired position in GEO. For Test 1 the optimization formulation is then:

$$\begin{aligned} \underset{\boldsymbol{X}}{\text{minimize}} \quad & J(\boldsymbol{X}) \\ \text{subject to} \quad & \dot{\mathbf{x}} = \mathbf{f}(t, \mathbf{x}), \\ & c_{eq1}(\boldsymbol{X}) = x_f - x_{GEO} = 0, \\ & c_{eq1}(\boldsymbol{X}) = y_f - y_{GEO} = 0 \end{aligned} \tag{68}$$

An inequality constraint is imposed in Tests 2-7 when a keep out zone is enforced. The time spent in the keep-out zone (t_{KOZ}) must be less than or equal to the time allowed in the keep out zone ($t_{allowed-KOZ}$):

$$\begin{aligned} \underset{\boldsymbol{X}}{\text{minimize}} \quad & J(\boldsymbol{X}) \\ \text{subject to} \quad & \dot{\mathbf{x}} = \mathbf{f}(t, \mathbf{x}), \\ & c_{eq1}(\boldsymbol{X}) = x_f - x_{GEO} = 0, \\ & c_{eq1}(\boldsymbol{X}) = y_f - y_{GEO} = 0, \\ & c(\boldsymbol{X}) = t_{KOZ} - t_{allowed-KOZ} \leq 0 \end{aligned} \tag{69}$$

3.6 Tests 6 and 7: Limiting Visual Magnitude

In Test 2-5 the detection range of the optical sensor is infinite. This will be modified to include a maximum detection range. The object being observed requires a minimum brightness magnitude to be detected by the optical sensor. This is known as the limiting visual magnitude. The brightness of the object is dependent on the solar phase angle, the material properties of the object, and the distance between the object and the optical sensor.

Current space-based sensors have a limiting visual magnitude of about 16.5 [6]. The characteristics for an object being observed will be replicated from [6]. Reference

[6] assumes an aluminum sphere with the materiel properties shown in Table 10. With the material properties defined and an assumed limiting visual magnitude, the maximum range of detection is a function of the solar phase angle ψ, shown in Eqs. (70)-(72) [33]. In equations (70)-(72), $\mathbf{v}$ is the vector from the observer to the satellite, $\mathbf{s}$ is the vector from the observer to the Sun, $p_{diff}(\phi)$ is the diffuse phase angle, a_{spec} and a_{diff} are the specular and diffuse components of reflectance, m_{sun} is the apparent magnitude of the Sun, and m_{lim} is the limiting visual magnitude of the optics.

$$\psi = cos^{-1}\Big(\frac{\mathbf{v}\cdot\mathbf{s}}{||\mathbf{v}||||\mathbf{s}||}\Big) \tag{70}$$

$$p_{diff}(\psi) = \frac{2}{3\pi}[sin(\psi) + (\pi - \psi)cos(\psi)] \tag{71}$$

$$\rho = \sqrt{\frac{d^2[a_{spec}/4 + a_{diff}p_{diff}(\psi)]}{10^{(m_{sun}-m_{lim})/2.5}}} \tag{72}$$

Table 10. Sensor and Satellite Properties

Diameter of Aluminum Sphere	0.5 meters (Test 6) and 1 meter (Test 7)
Aluminum Sphere Specular Reflectance	5 %
Aluminum Sphere Diffuse Reflectance	95 %
Limiting Magnitude of Optics	16.5

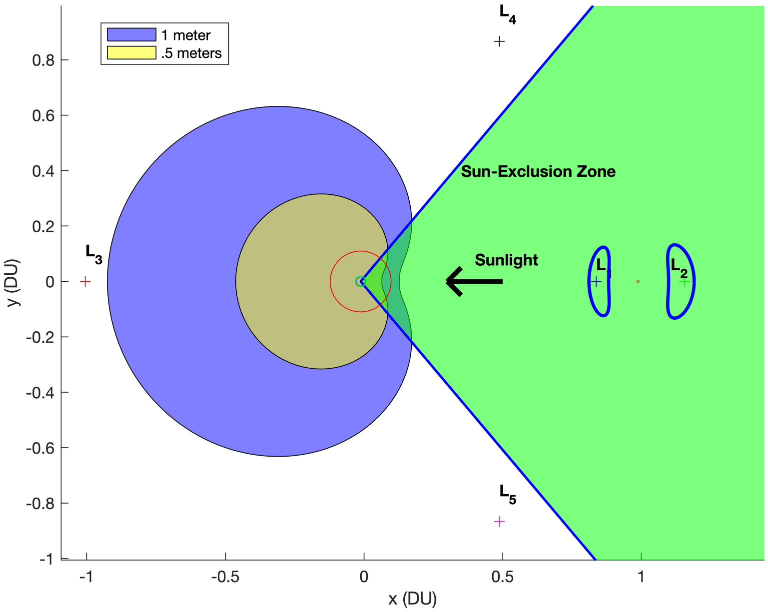

Figure 15. Limited Detection Range of Optical Sensor for 0.5 and 1 Meter Diameter Sphere

The new constraint in these tests will be to remain inside the Sun-exclusion zone, or remain outside of the maximum detection range during the transfer. Detection range adds another layer to consider when attempting to maintain custody of a satellite in cislunar space.

3.7 Summary

This chapter explained the research methodology to answer the research questions posed in Chapter 1. The problem scenario was described including the the L_1 and L_2 Lyapunov orbits, the Sun-exclusion zone, and limiting visual magnitude. This chapter explained the hybridization technique which will find the transfer solutions by optimizing fuel and time of flight.

IV. Results

4.1 Chapter Overview

Chapter 4 will go over the test results laid out in Chapter 3. The tests were performed using MATLAB® (R2018b). The computations were run on a MacBook Pro computer using a 2.7 GHz Intel® Core i5 with 8 GB of RAM.

The trajectory plots in this section will be colored in the following manner: starting/ending periodic orbits are drawn in **black**, unstable mainfolds are drawn in **blue**, and the TPBVP solutions are drawn in **green**.

4.1.1 Heteroclinic Connection.

The hybridization technique is first tested to find a heteroclinic connection between two periodic orbits to validate the optimization framework. A heteroclinic connection is a “free” transfer between two orbits by connecting the unstable manifold of one orbit to the stable manifold of another. Heteroclinic transfers first require the two periodic orbits to have matching Jacobi Constants. The technique to find heteroclinic connections is by propagating the unstable manifolds of the periodic orbit being departed from, and the stable manifolds of the destination periodic orbit. The unstable and stable manifolds are propagated in positive and negative time, respectively. Then a search is performed to find where there exists a matching state between a stable and unstable manifold, usually using a surface of section [1].

Another way of finding the heteroclinic connection is by using the hybridization technique described. If the hybridization technique is effectively performing a global search of the design space, the algorithm should find a minimum fuel solution with $\Delta V = 0$, or very close to zero. The work of Dahlke is recreated as a comparison [1]. Dahlke demonstrated that a pseudospectral method for optimal low-thrust trajectory design can converge onto a heteroclinic trajectory to find the minimum fuel solution [1]. The initial orbit is an L_1 periodic orbit and the target orbit a distant prograde orbit (DPO) about the Moon. These orbits are defined in Table 11.

Table 11. Heteroclinic Test Orbit Definition

	L_1 Periodic Orbit	DPO
x (DU)	0.812255	1.061692
y (DU)	0	0
$\dot{x}(DU/TU)$	0	0
$\dot{y}(DU/TU)$	0.248312	0.403877

The L_1 periodic orbit and DPO orbit are shown in Figure 16.

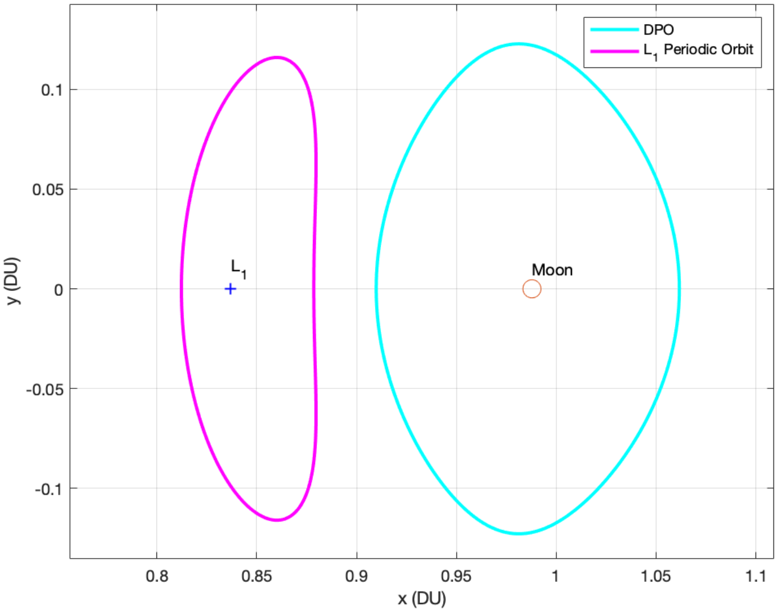

Figure 16. Orbits Used for Heteroclinic Transfer

A Pareto front is found using the GA and direct-method hybridization shown in Figure 17.

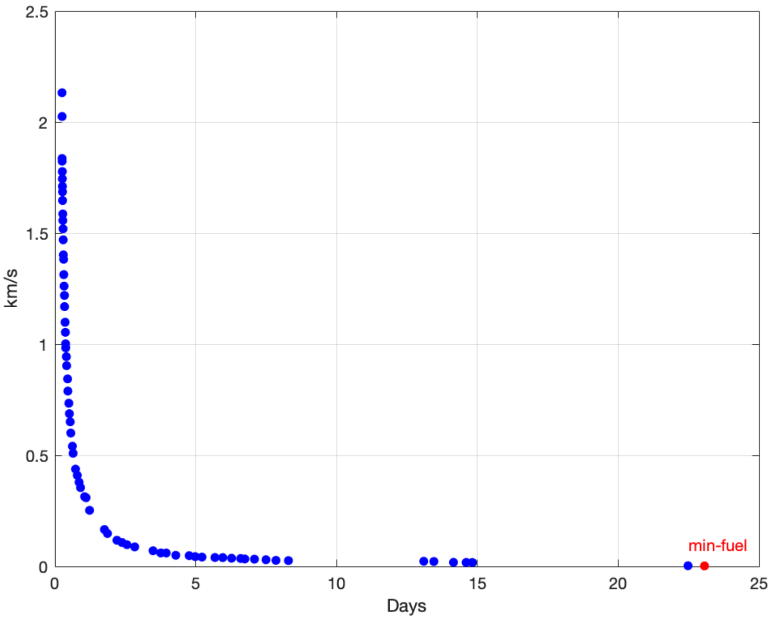

Figure 17. L_1 to DPO Pareto front

The red dot is the minimum fuel solution. If the technique is finding globally optimal solutions, this min-fuel solution should be very close to the heteroclinic trajectory. The trajectory path in Figure 18 is very similar to the heteroclinic connection found by Dahlke in Figure 19.

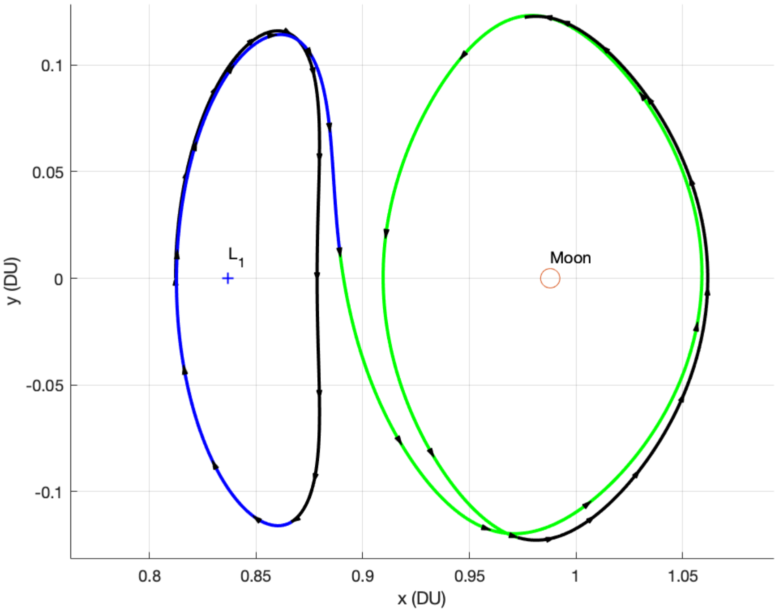

Figure 18. Min-Fuel Heteroclinic Connection Found Using Genetic Algorithm; starting/ending periodic orbits are drawn in black, unstable mainfolds are drawn in blue, and the TPBVP solutions are drawn in green

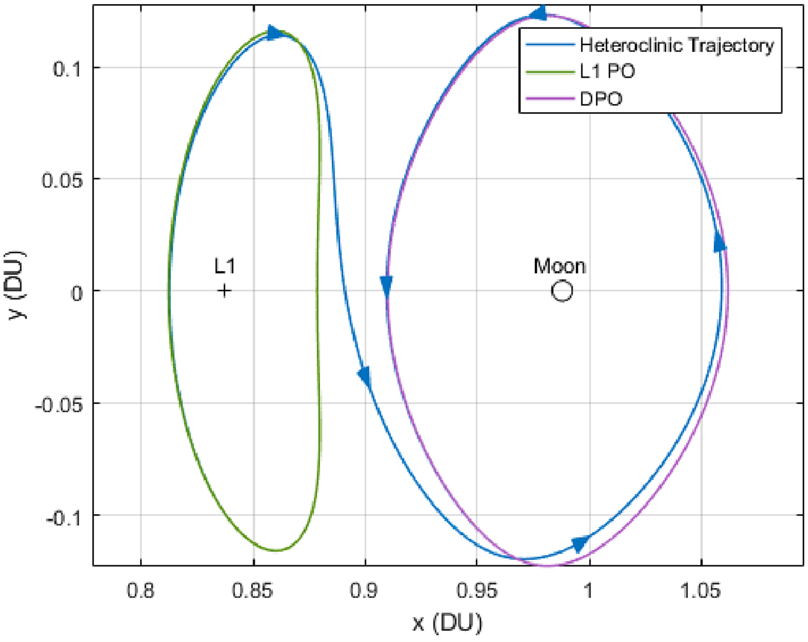

Figure 19. Heteroclinic Trajectory Found Between L_1 Periodic Orbit and DPO, Taken From [1]

The ΔV found is slightly higher than the one found by Dahlke. However, 2.3 m/s is small enough to conclude that a heteroclinic connection was found. Finding the heteroclinic connection here did not require an initial guess.

Table 12. Results Comparison

	Pseudospectral Method	GA
ΔV	0.8677 m/s	2.309 m/s
TOF	22 days	23.062 days

The test was repeated to find a heteroclinic connection between an L_1 Lyapunov orbit and an L_2 Lyapunov orbit with matching Jacobi Constants. The L_1 and L_2 Lyapunov orbits used here are the ones defined in Chapter 3 for the Lagrange to GEO transfer. The transfer was accomplished with 0.848 m/s of ΔV, and the transfer path is shown in Figure 20.

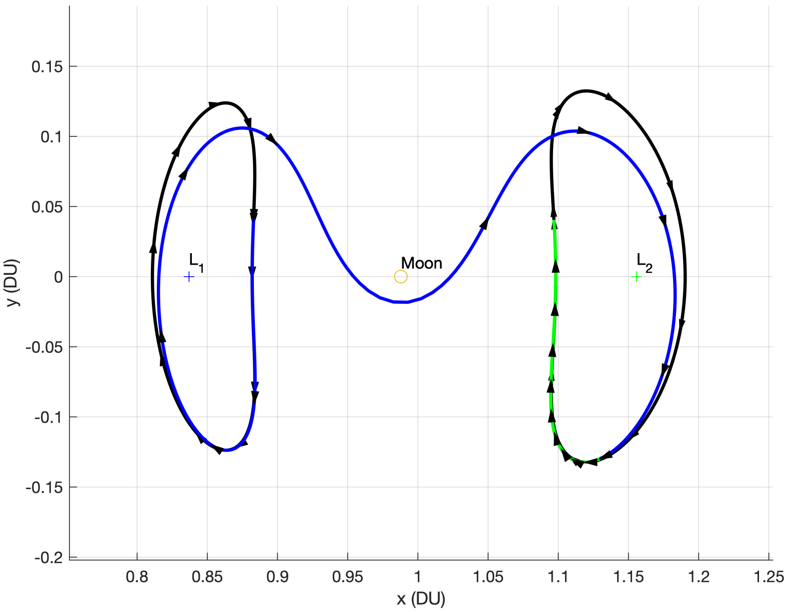

Figure 20. **L_1 to L_2 Lyapunov Heteroclinic Connection; starting/ending periodic orbits are drawn in black, unstable mainfolds are drawn in blue, and the TPBVP solutions are drawn in green.**

4.2 Results

4.2.1 Genetic Algorithm Settings.

Each generation of the genetic algorithm had a population size of 200, and each test used 50 generations. Fifty generations converged to a Pareto front, more generations did not improve the Pareto front by a significant amount. The *gamultiobj()* genetic operator settings were not altered from their default values. Figure 21 shows the generations progressing to the Pareto front, and illustrates the diminished returns past 50 generations. The problem being solved in Figure 21 is the transfer from the L_1 Lyapunov orbit to geosynchronous orbit.

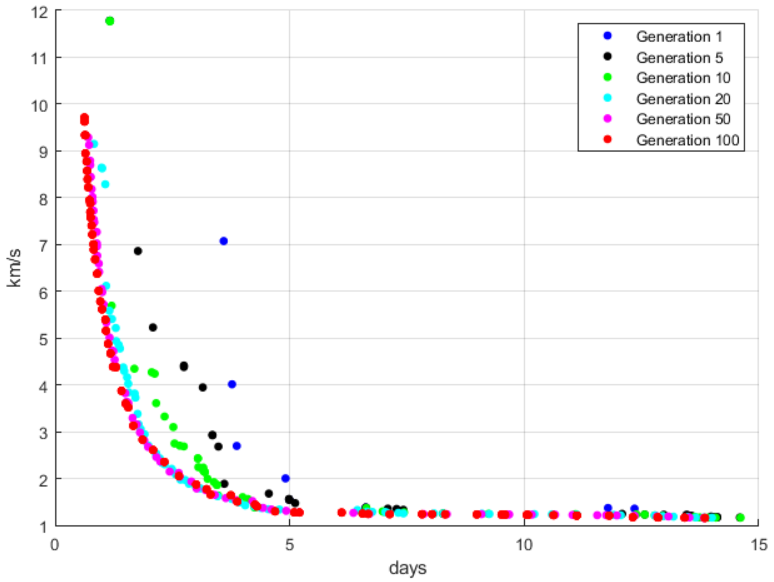

Figure 21. **L_1 Lyapunov Orbit to GEO Pareto Evolution**

For multimodal problems, an adequately large population size is important for finding solutions [34]. The population size was originally set to 50 but later increased to 200 with better results. The run time for the genetic algorithm to complete was long. The evaluation of each individual required the evaluation of a two point boundary value problem with *fmincon()*. Genetic algorithms lend themselves to parallel computing because each individual in a generation can be evaluated independently of the others (that is, parallel computation may further decrease the computation time). The type of problem being solved also affected run time. When the problem had Sun-exclusion zone constraints imposed, this typically increased run time. Run time increased when the problem involved a transfer through chaotic regions (that is, areas where small changes produce large effects over time). An L_2 to GEO transfer with Sun-exclusion zone constraints would take 24+ hours running in parallel. An L_1 to L_2 transfer with no Sun-exclusion zone constraints would take around 2 hours.

4.2.2 Test 1: Lyapunov Orbit to GEO Transfer, No SEZ Constraints.

Test 1 was concerned with finding the Pareto optimal solutions for a transfer from the L_1 and L_2 Lypaunov orbits to geosynchronous orbit. This test serves as a baseline comparison for Tests 2-7 when additional constraints are enforced. Shown below are the Pareto fronts produced in Test 1, as well as some sample transfers and additional plots to illustrate some of the characteristics of the solutions. Figure 22 shows the Test 1 results for both the L_1 and L_2 case.

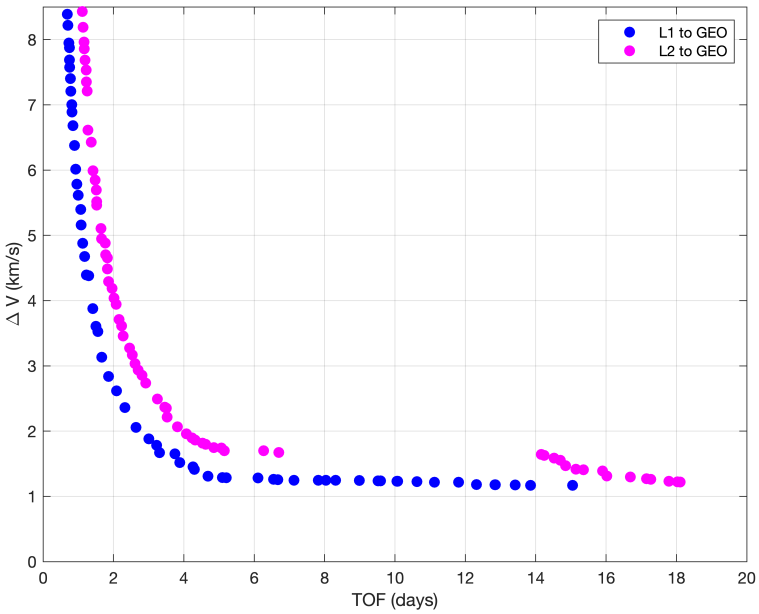

Figure 22. **L_1 and L_2 Lyapunov Orbit to GEO Transfer**

The L_1 Lyapunov to GEO case will be looked at closer. Figure 23 shows the Pareto front for the L_1 Lyapunov to GEO transfer, with specific solutions highlighted in green, yellow, and red. These specific solutions from the Pareto front are shown in Figures 24-26.

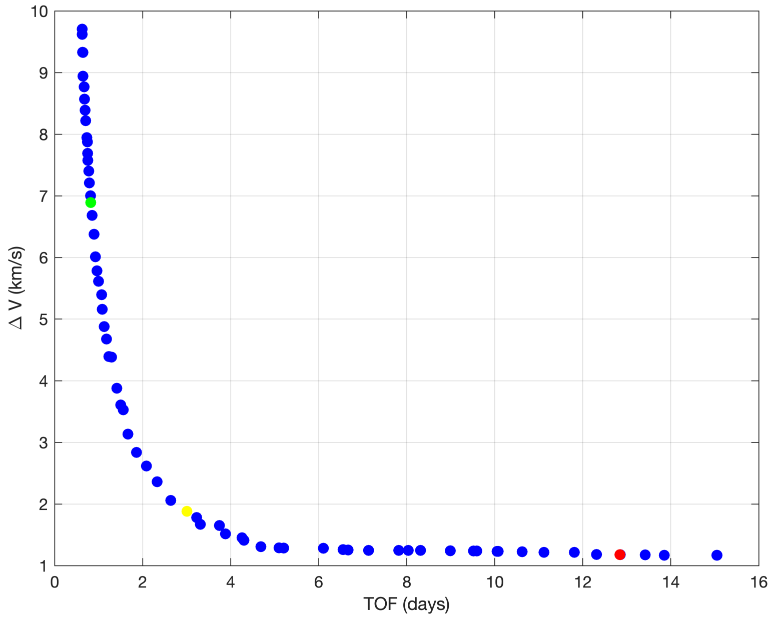

Figure 23. Pareto Front for L_1 to GEO Transfer, Plotted Transfers shown in Green, Yellow, and Red

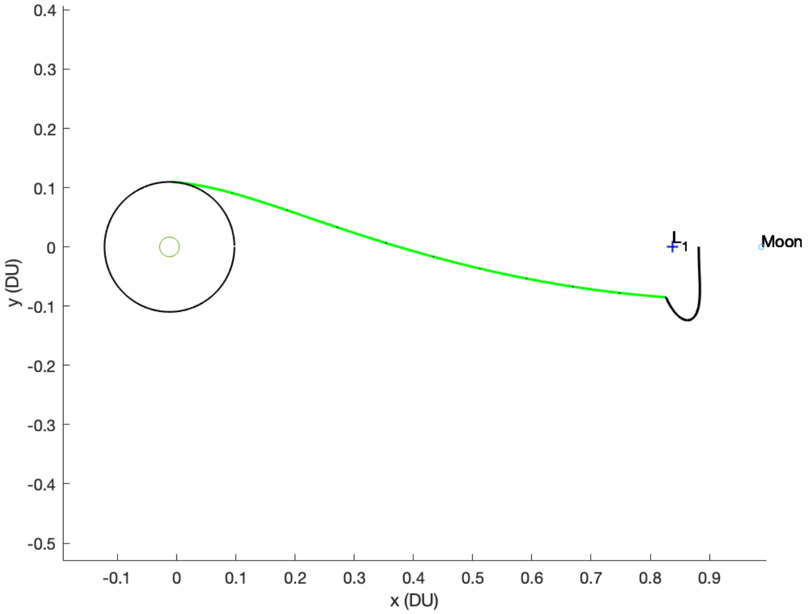

Figure 24. Green Transfer from Pareto Front in Figure 23; starting/ending periodic orbits are drawn in black, unstable mainfolds are drawn in blue, and the TPBVP solutions are drawn in green.

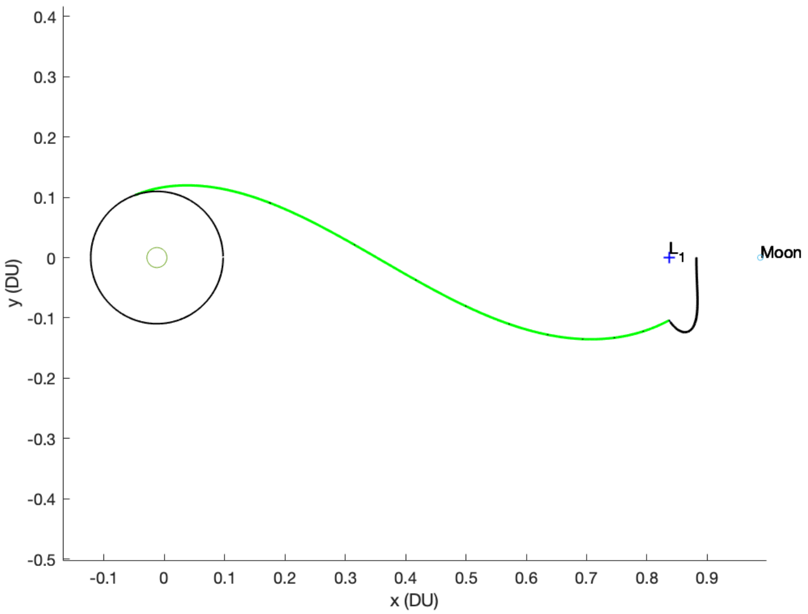

Figure 25. Yellow Transfer from Pareto Front in Figure 23; starting/ending periodic orbits are drawn in black, unstable mainfolds are drawn in blue, and the TPBVP solutions are drawn in green.

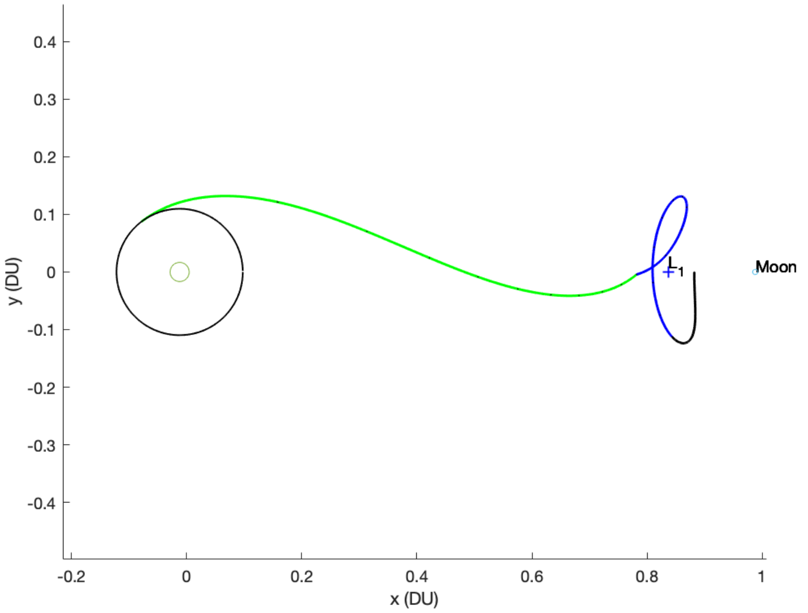

Figure 26. Red Transfer from Pareto Front in Figure 23; starting/ending periodic orbits are drawn in black, unstable mainfolds are drawn in blue, and the TPBVP solutions are drawn in green.

The invariant manifolds are used for transfers with longer time of flight and lower ΔV. Figure 27 shows the time spent on the invariant unstable manifold vs. the total ΔV. As is expected, the lower ΔV trajectories are those associated with longer times on the unstable manifold. The near vertical line in Figure 27 indicates that the low time of flight solutions spent significantly less time on the unstable manifold.

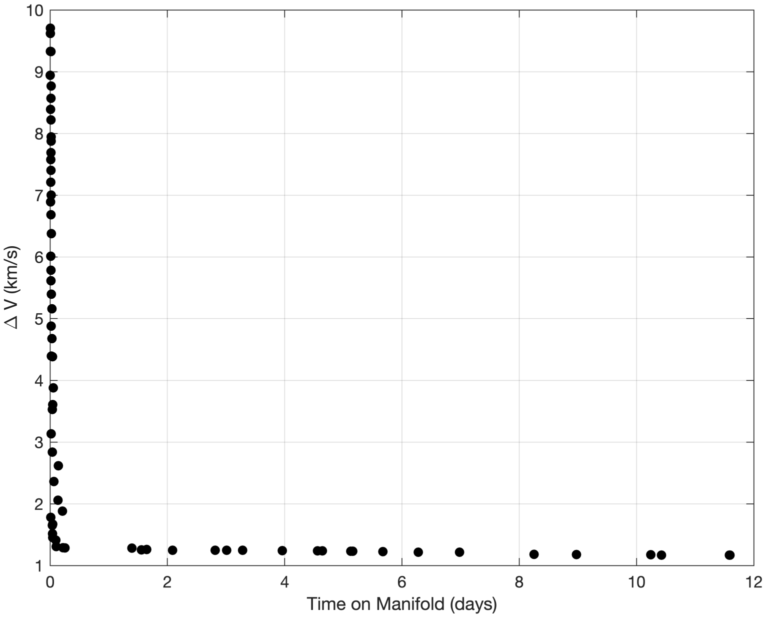

Figure 27. Total ΔV vs. Time on the Unstable Manifold

Figure 28 shows the relationship between the Pareto front and the location of insertion into Geosynchronous orbit, in the CR3BP frame.

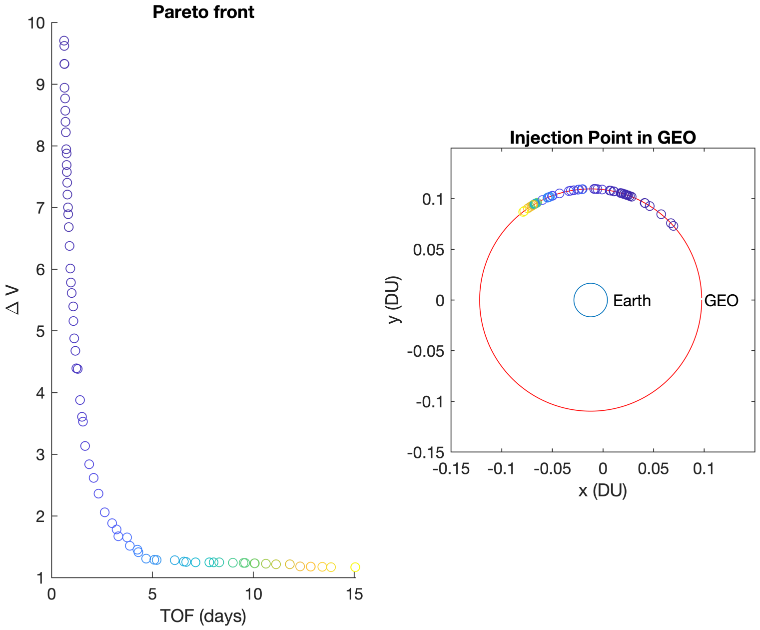

Figure 28. Comparing the Pareto Solutions to the Injection Point into Geosynchronous Orbit

4.2.3 Test 2-5: Lyapunov Orbit to GEO Transfer, SEZ Constraints.

In Test 2-5 the Sun-exclusion zone constraint is imposed. This constraint required that the transfer only spend a limited amount of time outside of the defined Sun-exclusion zone. This limited time ranged from 0 hours to 10 hours (0.096 in nondim time). The Pareto front solutions with this constraint are shown in Figures 29 and 30. The Pareto front without a Sun-exclusion zone constraint is also included to give a baseline comparison.

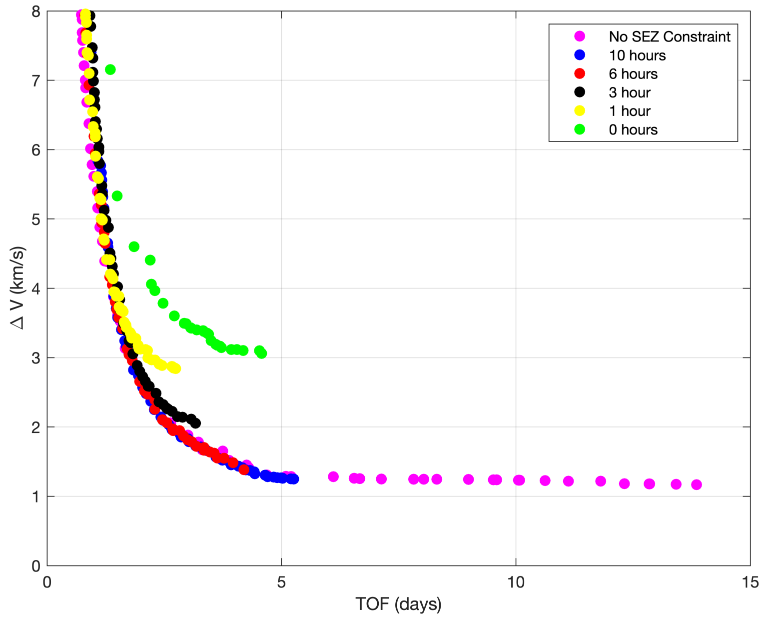

Figure 29. L_1 **to GEO Transfer**

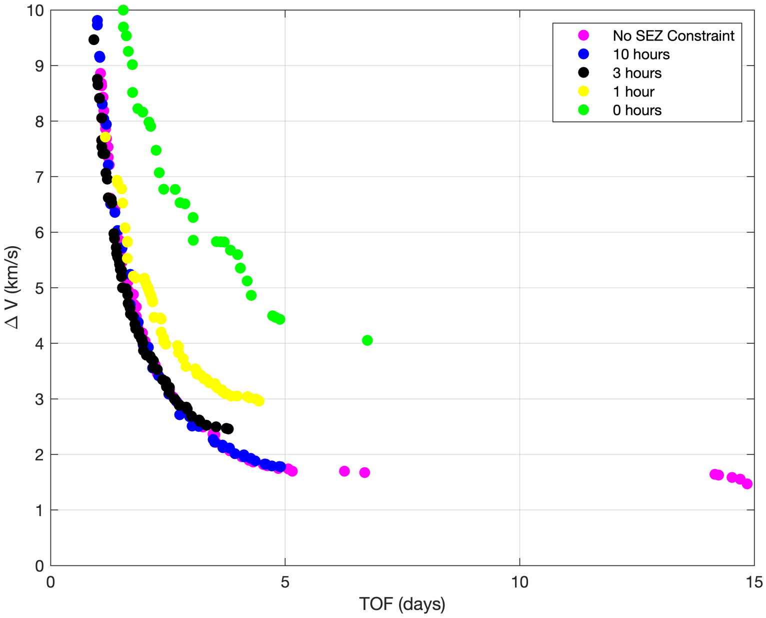

Figure 30. L_2 **to GEO Transfer**

The Pareto front sees a vertical shift with the more strict constraints, as is expected. Interestingly, the least restrictive constraint (10 hours) has solutions that lie along the unconstrained Pareto front. Although the 10-hour case had access to some of the original Pareto front, it did not have access to the longer time of flight/low ΔV solutions. It appears that these longer time of flight solutions were long enough that they could not remain in the Sun-exclusion zone for the duration of their transfer. As more restrictive constraints are imposed (decreasing the time allowed outside the SEZ), the Pareto front branches off of the baseline Pareto front. Eventually, as with the zero hour case, the problem is constrained enough that its Pareto front is completely removed from the baseline Pareto front.

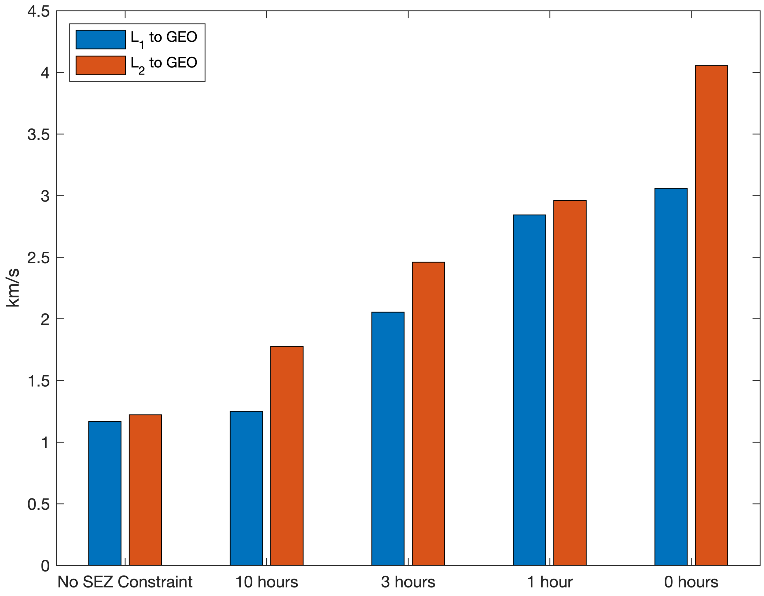

(a) ΔV Comparisons

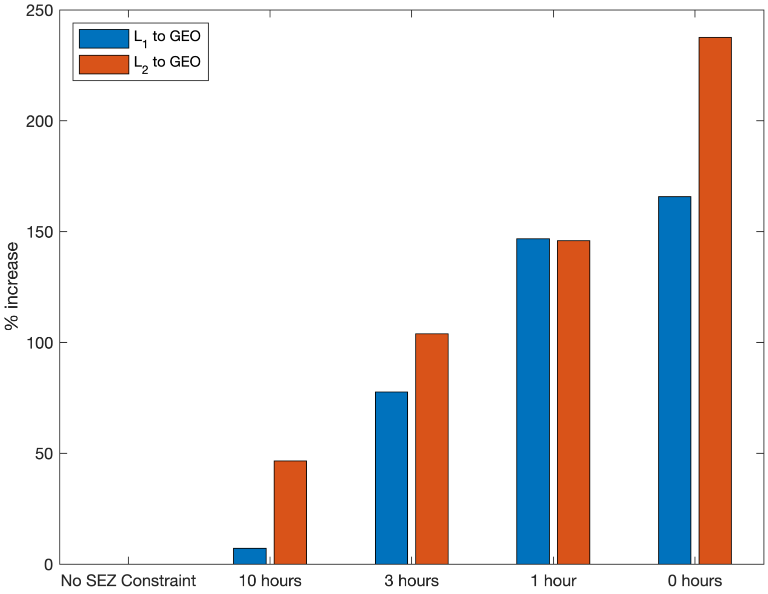

(b) ΔV Percentage Increase Over No SEZ Constraint Case

Figure 31. Min-Fuel Comparisons with Sun-Exclusion Zone Constraints

Figure 31 shows the trade off between time spent outside of the SEZ and ΔV. Without any Sun-exclusion zone constraints the transfer cost from L_1 and L_2 to GEO is about 1.25 km/s. This more than doubles if the constraint to remain inside the SEZ is imposed. However, if the constraint is only to spend *most* of the time inside the SEZ, this could be done with a reasonable ΔV cost increase. Since a satellite in GEO only spends 6 hours in the SEZ, it is inevitable the satellite will be outside of the SEZ soon after it arives in GEO.

The minimum fuel transfer for an L_2 Lyapunov orbit to GEO transfer while remaining inside of the SEZ is shown in Figure 32a. The SEZ when the satellite departs the Lyapunov orbit is shown by the green cone. The SEZ when the satellite arrives at GEO is shown in red. For comparison, a transfer with no SEZ constraint and a similar time of flight is shown in Figure 32b. This illustrates how the SEZ constraint is altering the transfer path.

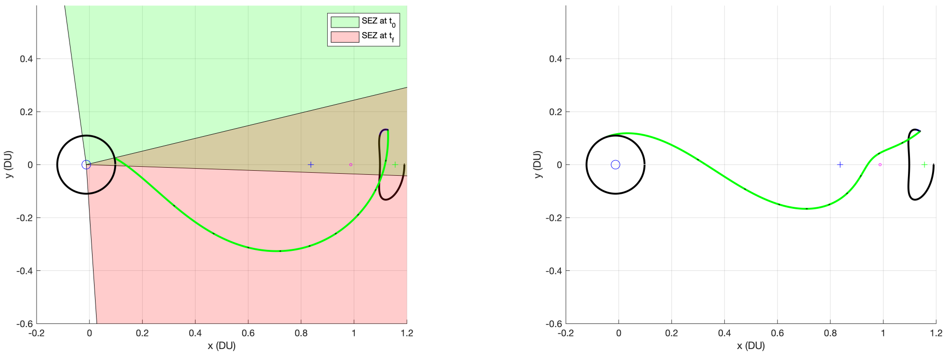

(a) Min-fuel Transfer With 0 hours Outside SEZ

(b) Comparible TOF L_2-GEO Transfer, No SEZ Constraint

Figure 32. Trajectory Comparison With and Without SEZ Constraint

4.2.4 Test 6-7: Lyapunov to GEO Transfer, SEZ Constraints, Limited Detection Range.

Tests 6-7 considers an L_1 and L_2 Lyapunov orbit to GEO transfer with a SEZ constraint and a limited detection range of the optical sensor. In this scenario, the transfer path is constrained to either a.) remain inside the SEZ b.) remain outside the maximum detection range, or c.) both a.) and b.). To define the maximum detection range the physical properties of the transferring satellite are assumed, and the optical sensor is given a limiting visual magnitude, shown in Table 10. The maximum detection range is then dependent on the solar phase angle shown in Eq. (72).

The results from Tests 6-7 are shown along with the results from Tests 1-5 in Figures 33 and 34.

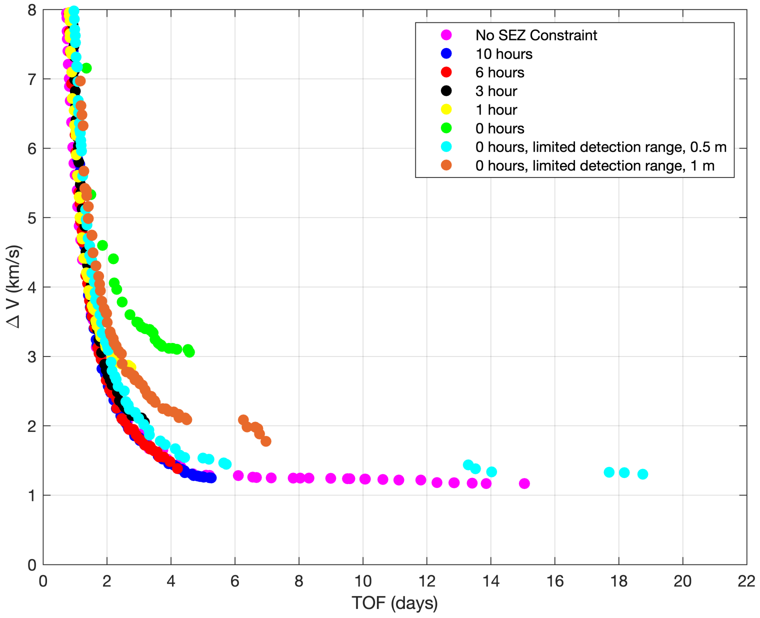

Figure 33. L_1 **Lyapunov-GEO Transfer**

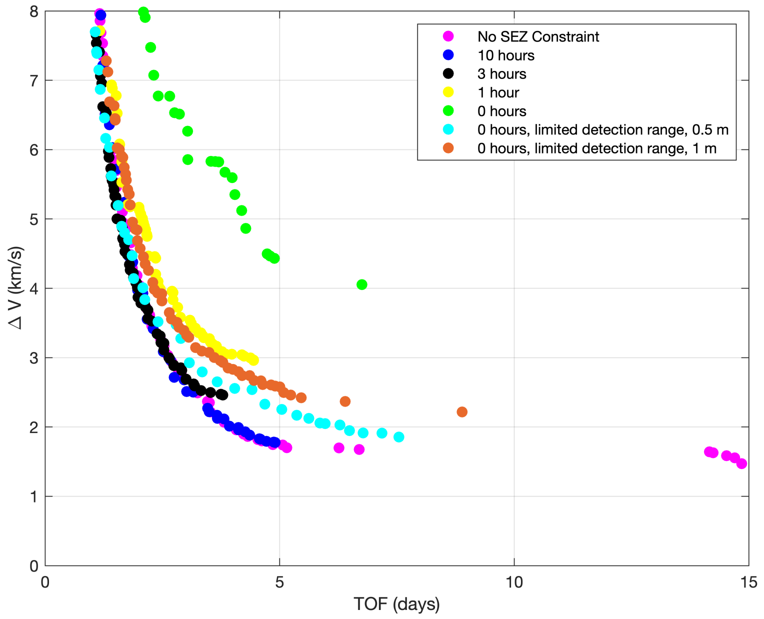

Figure 34. L_2 **Lyapunov-GEO Transfer**

The minimum fuel transfer in Test 7 from L_2 to GEO is shown in Figure 35. Because of the limited range, the solution is able to make use of the unstable manifold. The solution only needs to be concerned with the SEZ at lower altitudes within the detection range. The solution uses the SEZ for the end of the transfer.

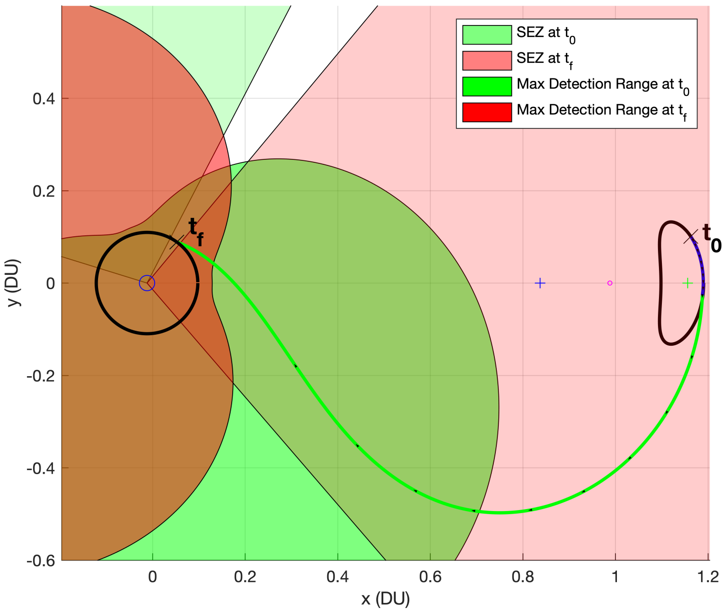

Figure 35. L_2-GEO Transfer; starting/ending periodic orbits are drawn in black, unstable manifolds are drawn in blue, and the TPBVP solutions are drawn in green.

Figure 36 shows the min-fuel transfer $\Delta V s$ of all seven test cases. The transfer is able to be made with a comparable ΔV to the unconstrained transfer case. Remaining inside of the SEZ to avoid detection by optical sensors may be most effective at lower altitudes, while at higher altitudes a satellite can avoid detection based on an optical sensor maximum detection range.

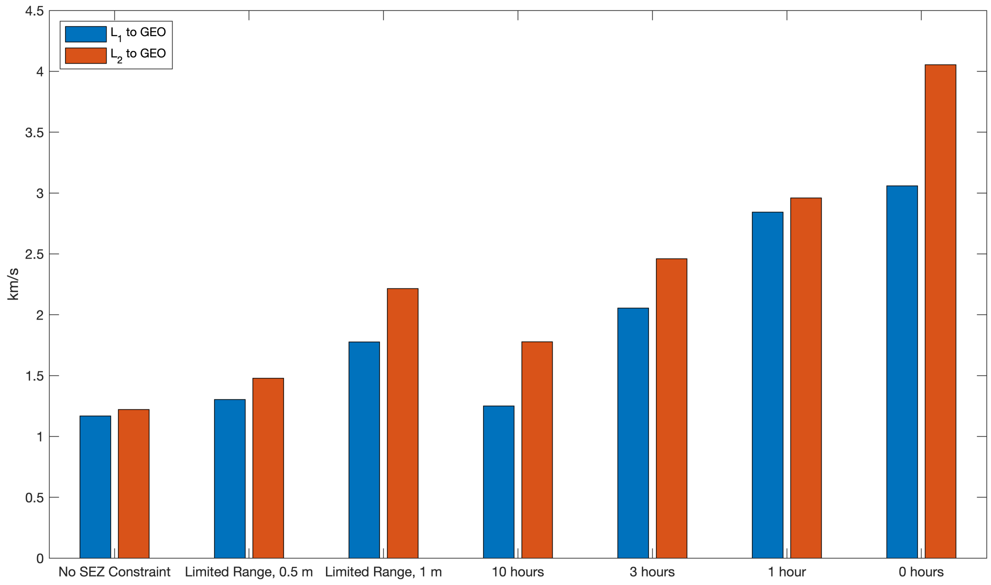

(a) ΔV Comparisons

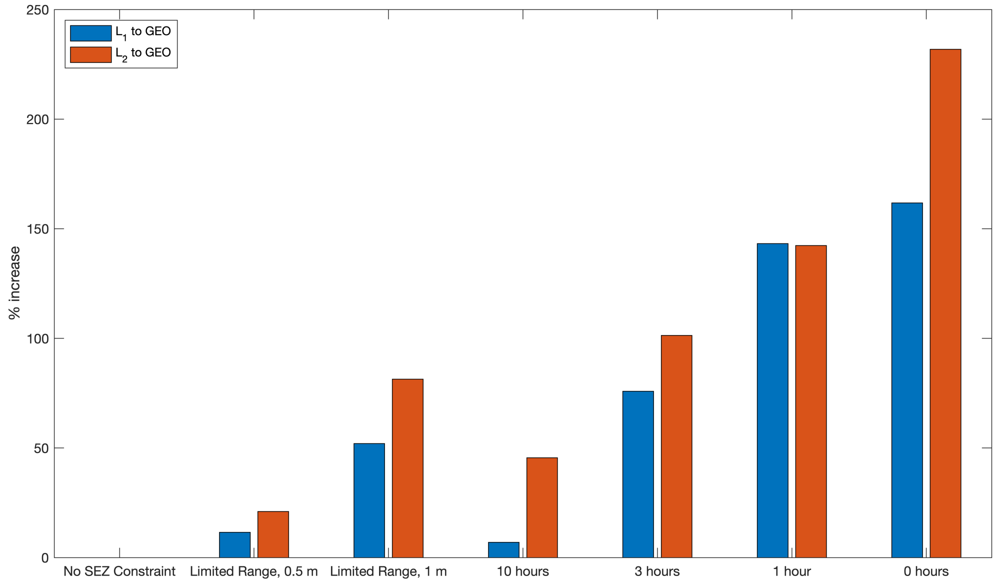

(b) ΔV Percentage Increase Over No SEZ Constraint Case

Figure 36. Min-fuel Comparisons with Sun-Exclusion Zone Constraints, Limited Range Included

4.3 Summary

This chapter demonstrated the genetic algorithm–direct method hybridization was able to find transfer solutions in the CR3BP. The hybridization was also shown to be capable of handling Sun-exclusion zone constraints.

Remaining inside the SEZ was shown to increase the required ΔV for the transfer significantly. For the L_1 and L_2 cases this required a 162% and 232% increase in ΔV, respectively. However, loosening this constraint allowed for lower ΔV transfers. Additionally, when the properties of the optical sensor and the target satellite were assumed and a maximum range determined, the transfer could be made more feasible. The 1 meter diameter sphere in the L_1 and L_2 cases required a 52% and 81% increase in ΔV, respectively. Overall, SEZ constraints on cislunar transfers to avoid detection by optical sensors can be prohibitive in terms of ΔV, but considering that the optical sensors have limited detection ranges can make the transfer more feasible.

V. Conclusions and Recommendations

5.1 Summary of Work

The current work evaluated how effectively, in terms of fuel and transfer time, a satellite could make a transfer from an orbit near the Moon to Earth while remaining in the Sun-exclusion zone for an optical sensor near the Earth. The research used a hybridization between a genetic algorithm, MATLAB's *gamultiobj()*, and a direct method, MATLAB's *fmincon()*, to find solutions in the Circular Restricted Three Body Problem. The method found Pareto optimal solutions weighing the objectives time of flight and ΔV. A satellite would remain unobserved by optical sesnors while remaining inside of a sensor's Sun-exclusion zone.

The hybridization technique was used to find heteroclinic connections, demonstrating the ability to find optimal solutions. The technique was able to find these solutions with considerably low ΔV. Finding these heteroclinic connections did not require an initial guess, making this method robust for solving problems in the CR3BP.

In the first test, the hybridization technique found Pareto optimal solutions for a transfer from L_1 and L_2 Lyapunov orbits to geosynchronous orbit with Sun-exclusion zone constraints. This scenario created a baseline Pareto front to which the future tests would be compared. These transfers used the unstable manifolds in the CR3BP to find low-fuel solutions.

In Tests 2-5, the transfer was constrained to remain inside of a Sun-exclusion zone. Remaining completely inside of the SEZ considerably increased the total ΔV in the minimum fuel case. A Moon to Earth transfer is possible while remaining in the Sun-exclusion zone, but with considerable cost in terms of fuel. For the L_1 and L_2 cases it caused a 162% and 232% increase in ΔV, respectively. This much of an increase in ΔV makes the transfers much less desirable.

In Tests 6 and 7, the transfer was constrained to remain inside of the SEZ, or remain outside of a defined maximum detection range of the optical sensor. This made the transfer solutions cheaper in terms of ΔV. For the L_1 and L_2 cases for a 1 meter diameter sphere, a 52% and 81% increase in ΔV was required, respectively.

5.2 Contributions

In Chapter 1 the following research questions were asked:

1. Can a genetic algorithm–direct method generate transfers from L_1 and L_2 Lyapunov orbits to geosynchronous orbit while optimizing fuel and time of flight?
2. What is the feasibility of making transfers from L_1 and L_2 Lyapunov orbits to GEO while enforcing a constraint that the transfer must remain inside of a Sun-exclusion zone?

For the first question, the hybridization demonstrated it was able to solve for transfers from L_1 and L_2 Lyapunov orbits to GEO while optimizing fuel and time of flight. Pareto fronts were generated to show the trade space between the objectives in Section 4.2.2.

The hybridization was shown to effectively solve for transfers starting at L_1 and L_2 Lyapunov orbits and ending at geosynchonous orbit while handling Sun-exclusion zone constraints, shown in Section 4.2.3. Remaining inside of a SEZ during the transfer was shown to significantly increase the ΔV for the min-fuel transfer case. Relaxing the constraint made the transfers more feasible, shown in Section 4.2.4. When considering that the optical sensors have a maximum detection range, the transfer was shown to be more feasible in terms of fuel. To answer the second research question, the transfer with SEZ constraints is possible, but would require a large increase in ΔV. However, when considering a maximum detection range of the optical sensor, the transfer can be made with a smaller ΔV budget. The cost in terms of ΔV over the unconstrained case is shown in Figure 36. All optical sensors will suffer from a Sun-exclusion zone. Optical sensors have significant periods where they are unable to observe satellites in geosynchronous orbit due to the SEZ. Along the same line, optical sensors are limited in their ability to observe certain cislunar trajectories. The current research provides a methodology for creating optimal cislunar trajectories with SEZ constraints enforced, and provides insight into the limitation of near-Earth optical sensors to detect cislunar trajectories.

5.3 Future Work

Future work could include:

- Future tests can include continuous thrust instead of impulsive thrust. Continuous thrust would enable active control during the entire transfer to satisfy constraints. Continuous thrust transfers could offer lower ΔV solutions.
- The spatial, instead of the planar, circular restricted three body problem could be considered. Instead of targeting geosynchronous orbit, the target orbit could be geostationary orbit.
- The solutions recreated in a higher fidelity ephemeris model. This would serve to check if the trajectories hold up with the additional perturbations and the removal of CR3BP assumptions.
- Additional optical observers can be added to the problem. Additional observers create independent Sun-exclusion zones. For the observation system consisting of several sensors, the Sun-exclusion zone would be the overlapping region of all sensors included. Instead of considering just one observer near the Earth,

observers at higher altitudes like GEO or at a Lagrange point could be considered.

Bibliography

1. J. A. Dahlke, "Optimal Trajectory Generation in a Dynamic Multi-Body Environment Using a Pseudospectral Method," Master's thesis, Air Force Institute of Technology, 2018.
2. R. M. Gates and J. R. Clapper, "National Security Space Strategy Unclassified Summary," *Washington DC: US Department of Defense and Office of the Director of National Intelligence*, 2011.
3. "Space Operations, Joint Publication 3-14," *Joint Chiefs of Staff*, 2018.
4. D. J. Trump, "National Security Strategy of the United States of America," Executive Office of The President Washington DC Washington United States, Tech. Rep., 2017.
5. E. P. Chatters and B. J. Crothers, "Space Surveillance Network," *AU-18 Space Primer*, pp. 249–258, 2009.
6. D. A. Vallado, P. J. Cefola, R. Kiziah, and M. Ackermann, "Removing the Solar Exclusion with High Altitude Satellites," in *AIAA/AAS Astrodynamics Specialist Conference*, 2016.
7. J. N. Brick, "Military Space Mission Design and Analysis in a Multi-Body Environment: An Investigation of High-Altitude Orbits as Alternative Transfer Paths, Parking Orbits for Reconstitution, and Unconventional Mission Orbits," Master's thesis, Air Force Institute of Technology, 2017.
8. M. Kakoi, "Design of Transfers from Earth-Moon L1/L2 Libration Point Orbits to a Destination Object," Ph.D. dissertation, Purdue University, 2015.

9. M. Lo, B. Williams, W. Bollman, D. Han, Y. Hahn, J. Bell, E. Hirst, R. Corwin, P. Hong, and K. Howell, "Genesis Mission Design," in *AIAA/AAS Astrodynamics Specialist Conference and Exhibit*, 1998.

10. R. Whitley and R. Martinez, "Options for Staging Orbits in Cislunar Space," in *2016 IEEE Aerospace Conference.* IEEE, 2016, pp. 1–9.

11. B. A. Conway, *Spacecraft Trajectory Optimization.* Cambridge University Press, 2010.

12. K. Meyer, G. Hall, and D. Offin, *Introduction to Hamiltonian Dynamical Systems and the N-body Problem.* Springer Science & Business Media, 2008.

13. V. Szebehely, *Theory of Orbit: The Restricted Problem of Three Bodies.* Elsevier, 1967.

14. T. A. Pavlak, "Trajectory Design and Orbit Maintenance Strategies in Multi-Body Dynamical Regimes," Ph.D. dissertation, Purdue University, 2013.

15. L. Euler, "De motu rectilineo trium corporum se mutuo attrahentium," *Novi Comm. Acad. Sci. Imp. Petrop*, vol. 11, pp. 144–151, 1767.

16. J. Lagrange, "Essay on The Problem of Three Bodies," *Works of Lagrange*, vol. 6, pp. 229–331, 1772.

17. G. Gomez, W. S. Koon, M. W. Lo, J. E. Marsden, J. Masdemont, and S. D. Ross, *Invariant Manifolds, the Spatial Three-Body Problem and Space Mission Design.* American Astronautical Society, 2001.

18. W. E. Wiesel, *Modern Astrodynamics.* Aphelion Press Beavercreek, OH, 2010.

19. W. S. Koon, M. W. Lo, J. E. Marsden, and S. D. Ross, “Dynamical Systems, the Three-Body Problem and Space Mission Design,” *California Institute of Technology, Pasadena, CA, USA*, 2006.

20. B. Barden, K. Howell, and M. Lo, “Application of Dynamical Systems Theory to Trajectory Design for a Libration Point Mission,” in *AIAA/AAS Astrodynamics Conference*, 1996.

21. M. Vavrina and K. Howell, “Global Low-Thrust Trajectory Optimization Through Hybridization of a Genetic Algorithm and a Direct Method,” in *AIAA/AAS Astrodynamics Specialist Conference and Exhibit*, 2008.

22. J. T. Betts, “Survey of Numerical Methods for Trajectory Optimization,” *Journal of Guidance, Control, and Dynamics*, vol. 21, no. 2, pp. 193–207, 1998.

23. A. Shirazi, J. Ceberio, and J. A. Lozano, “Spacecraft Trajectory Optimization: A Review of Models, Objectives, Approaches and Solutions,” *Progress in Aerospace Sciences*, vol. 102, pp. 76–98, 2018.

24. V. Coverstone-Carroll, J. Hartmann, S. Williams, and W. Mason, “New Results in Astrodynamics Using Genetic Algorithms,” 1998.

25. V. J. Shah, “Automated Global Optimization of Low-Energy Trajectories Using a Hybrid Optimal Control Framework,” Master’s thesis, University of Illinois, 2017.

26. P. Moscato *et al.*, “On Evolution, Search, Optimization, Genetic Algorithms and Martial Arts: Towards Memetic Algorithms,” *Caltech Concurrent Computation Program, C3P Report*, 1989.

27. S. Hatch, M.-k. Chung, J. Kangas, S. Long, R. Roncoli, and T. Sweetser, “Trans-Lunar Cruise Trajectory Design of GRAIL (Gravity Recovery and Interior Laboratory) Mission,” in *AIAA/AAS Astrodynamics Specialist Conference*, 2010.

28. P. Cage, I. Kroo, and R. Braun, “Interplanetary Trajectory Optimization Using a Genetic Algorithm,” in *AIAA/AAS Astrodynamics Conference*, 1994.

29. D. T. Bunce, “Spacecraft Trajectory Design Utilizing Resonance Orbits in a Hybrid Optimal Control Framework,” Master’s thesis, University of Illinois, 2017.

30. M. R. Ackermann, C. Kiziah, P. Zimmer, J. McGraw, and D. Cox, “A Systematic Examination of Ground-Based and Space Based Approaches to Optical Detection and Tracking of Satellites,” in *31st Space Symposium*, 2015.

31. G. H. Stokes, H. E. Viggh, and J. K. Pollock, “Space-Based Visible (SBV) Surveillance Data Verification and Telemetry Processing,” in *International Telemetering Conference Proceedings*. International Foundation for Telemetering, 1996.

32. D. Izzo, “Revisiting Lamberts problem,” *Celestial Mechanics and Dynamical Astronomy*, vol. 121, no. 1, pp. 1–15, 2015.

33. J. L. Worthy III, M. J. Holzinger, and K. Fujimoto, “Optical Sensor Constraints on Space Object Detection and Admissible Regions,” in *Paper AAS 13-707 presented at the AAS/AIAA Astrodynamics Specialist Conference*, 2013.

34. K. Deb and S. Agrawal, “Understanding Interactions among Genetic Algorithm Parameters.” in *FOGA*, 1998, pp. 265–286.

REPORT DOCUMENTATION PAGE

Form Approved
OMB No. 0704–0188

1. REPORT DATE *(DD–MM–YYYY)* 10–02–2013	**2. REPORT TYPE** Master's Thesis	**3. DATES COVERED** *(From — To)* Sept 2011 — Mar 2013

4. TITLE AND SUBTITLE

AFIT/ENP THESIS PRIMER:
A DOCUMENT IN LaTeX

5a. CONTRACT NUMBER

5b. GRANT NUMBER

5c. PROGRAM ELEMENT NUMBER

6. AUTHOR(S)

Joshua A. Ostman

5d. PROJECT NUMBER

5e. TASK NUMBER

5f. WORK UNIT NUMBER

7. PERFORMING ORGANIZATION NAME(S) AND ADDRESS(ES)

Air Force Institute of Technology
Graduate School of Engineering and Management (AFIT/EN)
2950 Hobson Way
WPAFB OH 45433-7765

8. PERFORMING ORGANIZATION REPORT NUMBER

AFIT/GAP/ENP/11-S01

9. SPONSORING / MONITORING AGENCY NAME(S) AND ADDRESS(ES)

Department of Engineering Physics
2950 Hobson Way
WPAFB OH 45433-7765
DSN 271-0690, COMM 937-255-3636
Email: amy.magnus@afit.edu

10. SPONSOR/MONITOR'S ACRONYM(S)

AFWA

11. SPONSOR/MONITOR'S REPORT NUMBER(S)

12. DISTRIBUTION / AVAILABILITY STATEMENT

DISTRIBUTION STATEMENT A:
APPROVED FOR PUBLIC RELEASE; DISTRIBUTION UNLIMITED.

13. SUPPLEMENTARY NOTES

14. ABSTRACT

This primer aids the AFIT student in generating the first draft of their thesis using LaTeX. The primer is produced according the tenets described within the document. All source code is provided in a zip file posted to L:\Courses\PHYS\LaTeX. The file structure of this zip file demonstrates a practical way to organize a thesis with its supporting materials and—further—illustrates how your document can be produced with version control.

15. SUBJECT TERMS

LaTeX,Thesis

16. SECURITY CLASSIFICATION OF:			**17. LIMITATION OF ABSTRACT**	**18. NUMBER OF PAGES**	**19a. NAME OF RESPONSIBLE PERSON**
a. REPORT	**b. ABSTRACT**	**c. THIS PAGE**			Dr. I. M. Smart, AFIT/ENP
U	U	U	U	110	**19b. TELEPHONE NUMBER** *(include area code)* (937) 255-3636, x4555; amy.magnus@afit.edu

Standard Form 298 (Rev. 8–98)
Prescribed by ANSI Std. Z39.18